Fat3 acts through independent cytoskeletal effectors to coordinate asymmetric cell behaviors during polarized circuit assembly

Evelyn C. Avilés[1], Alexandra Krol[1], Steven J. Henle[1,4], Jessica Burroughs-Garcia[2], Michael R. Deans[2,3], Lisa V. Goodrich[1,5,*]

[1]Department of Neurobiology, Harvard Medical School, Boston, MA 02115, USA

[2]Department of Neurobiology, University of Utah School of Medicine, Salt Lake City, UT 84112, USA

[3]Department of Surgery, Division of Otolaryngology – Head and Neck Surgery, University of Utah School of Medicine, Salt Lake City, UT 84132, USA

[4]Present address: Department of Neuroscience, Carthage College, 2001 Alford Park Dr., Kenosha, WI 53140, USA

[5]Lead contact

SUMMARY

The polarized flow of information through neural circuits depends on the orderly arrangement of neurons, their processes, and their synapses. This polarity emerges sequentially in development, starting with the directed migration of neuronal precursors, which subsequently elaborate neurites that form synapses in specific locations. In other organs, Fat cadherins sense the position and then polarize individual cells by inducing localized changes in the cytoskeleton that are coordinated across the tissue. Here, we show that the Fat-related protein Fat3 plays an analogous role during the assembly of polarized circuits in the murine retina. We find that the Fat3 intracellular domain (ICD) binds to cytoskeletal regulators and synaptic proteins, with discrete motifs required for amacrine cell migration and neurite retraction. Moreover, upon ICD deletion, extra neurites form but do not make ectopic synapses, suggesting that Fat3 independently regulates synapse localization. Thus, Fat3 serves as a molecular node to coordinate asymmetric cell behaviors across development.

Graphical abstract

In brief

Avilés et al. show that the atypical cadherin Fat3 acts in a modular fashion to coordinate the assembly of polarized circuits in the retina. Amacrine cell migration, neurite retraction, and synapse localization require different sets of motifs in the intracellular domain, with a prominent role for recruitment of the WRC.

INTRODUCTION

A fundamental feature of the nervous system is the directed flow of signals through interconnected networks of neurons. Directionality is achieved by morphological asymmetries in the neurons, which receive signals through dendrites and send signals through axons. There is also polarity at the level of the circuit such that neurons and their processes are properly positioned with respect to each other and to the axes of the nervous system. To create a polarized circuit, developing neurons must migrate to the correct location, which requires transient polarization, and then generate and maintain polarized morphologies, including the formation of spatially restricted synapses. Polarization depends on intrinsic changes in cytoskeletal organization that differentiate the leading process from the trailing process in migrating neurons (Jossin, 2020) and cause one neurite to become an axon in mature neurons (Barnes and Polleux, 2009). However, little is known about how these intrinsic changes are coordinated across the developing circuit.

The orderly alignment of neurons within circuits is reminiscent of the phenomenon of tissue polarity. Best understood in *Drosophila*, tissue polarity is controlled by two signaling systems: the "core" planar cell polarity (PCP) pathway and the Fat/Dachsous system (Goodrich and Strutt, 2011). Both pathways establish asymmetric protein distributions that are propagated to neigh-boring cells, ultimately localizing intracellular effectors and thereby creating morphological asymmetries while simultaneously aligning these asymmetries across the field of cells. Originally identified for its ability to polarize cells in the plane of an epithelium, the core PCP pathway also enables the asymmetric growth of axons and the assembly of synapses, which are fundamentally asymmetric structures (Zou, 2020). The Fat/Dachsous system coordinates polarity in a variety of epithelial structures across species and in many tissues. Fat is an atypical single-pass cadherin that interacts with a related cadherin, Dachsous, to induce asymmetries that are aligned among cells, with Fat4 and Dsch1 playing conserved roles in vertebrates (Mao et al., 2011). The closely related Fat-like cadherin also orients cell behavior by inducing local changes in the cytoskeleton, as shown for collective cell migration in the *Drosophila* egg chamber (Barlan et al., 2017; Chen et al., 2016; Squarr et al., 2016; Viktorinová et al., 2009). Fat-like's effects on polarity do not depend on Dachsous (Viktorinová et al., 2009), and no ligands for its vertebrate orthologs Fat1 and Fat3 have been described. In vertebrates, Fat1, Fat3, and Fat4 act both synergistically and independently to organize tissue morphogenesis, growth, and cell migration, including in the nervous system (Badouel et al., 2015; Cappello et al., 2013; Deans et al., 2011; Gee et al., 2016; Hou et al., 2006; Krol et al., 2016; Miyazaki, 2011; Moeller et al., 2004; Tanoue and Takeichi, 2004; Zakaria et al., 2014).

Fat cadherins are single-pass transmembrane molecules that signal through multiple independent pathways to elicit effects on cell growth, shape, and metabolism (Fulford and McNeill, 2020). Versatility depends in part on the intracellular domain (ICD), which interacts with a variety of cytoplasmic effectors via discrete domains (Sadeqzadeh et al., 2014). Effects on tissue polarity require interactions with cytoskeletal regulators that create local changes in cell shape, a property that is observed even in evolutionarily ancient Fat cadherins (Brooun et al., 2020). Additional functional versatility is achieved by their huge extracellular domain (ECD), which receives signals and also acts non-autonomously to influence the behavior of surrounding cells (Barlan et al., 2017). In addition, both the ECD and ICD are important for Fat's asymmetric localization, as is common for tissue polarity systems.

Growing evidence suggests that Fat cadherins play analogous tissue polarity roles during neural circuit assembly (Avilés and Goodrich, 2017). These effects are well illustrated in the retina, where amacrine cells (ACs) send visual information from photo-receptors in the outer nuclear layer (ONL) to retinal ganglion cells (RGCs) in the ganglion cell layer (GCL) via synapses in the inner plexiform layer (IPL). During development, newborn ACs migrate through the neuroblast layer (NBL) to reach the inner nuclear layer (INL), with a subset continuing to the GCL. Upon reaching the appropriate location, ACs retract neurites that are outside of the IPL, elaborating one main dendritic arbor that forms synapses restricted to the IPL (Deans et al., 2011; Ray et al., 2018). Fat3 is asymmetrically localized to the neurites in the nascent IPL (Deans et al., 2011; Nagae et al., 2007), highlighting parallels with its role in classic tissue polarity. Indeed, both the overall organization of the retina

and the polarized behaviors of developing ACs are disrupted in *Fat3* mutant mice. Rather than migrating in a directed fashion, *Fat3* mutant ACs vacillate and often fail to migrate to the appropriate location (Krol et al., 2016). Additionally, neurites outside of the IPL are not reliably retracted and form synapses that create two misplaced plexiform layers, one interrupting the INL and one under the GCL (Deans et al., 2011). Thus, Fat3 coordinates multiple stages of AC behavior needed for the formation of layers and, hence, the directed flow of visual information.

Like other Fat-related proteins, Fat3 interacts with a variety of intracellular effectors that could contribute to its ability to create asymmetric cell shapes. For instance, the Fat3-ICD binds to the Kinesin-1 component Kif5B (Cheng et al., 2016) and harbors binding sites for two sets of actin regulatory molecules, the Ena/VASP proteins (Krol et al., 2016) and the WAVE regulatory complex (WRC) (Chen et al., 2014a). Ena/VASP proteins are mislocalized in *Fat3* mutant ACs, and the forced redistribution of Ena/VASP proteins is sufficient to prevent neurite retraction (Krol et al., 2016). How the WRC contributes to Fat3 function is unclear, but interactions with the WRC are important for Fat-like's effects on collective cell migration in flies (Squarr et al., 2016). WRC-interacting receptor sequence (WIRS) motifs are also present in several synaptogenic receptors (Chen et al., 2014a), and the localization of the WRC is important for synapse formation in worms (Chia et al., 2014). Thus, it is possible that Fat3 acts through independent sets of effectors to induce changes in the cytoskeleton that are needed for directed migration, neurite retraction, and synapse localization.

Here, we investigated how Fat3's molecular versatility is harnessed to organize circuit assembly at the tissue level. We found that the Fat3-ICD interacts with many molecules associated with cytoskeletal regulation and synapse development. Deletion of discrete motifs disrupted binding to predicted effectors selectively. Further, the composition of the Fat3-ICD seems to differ in migrating versus differentiating ACs such that different effectors could be used at each stage. Indeed, AC migration requires the Kif5 interaction domain (Kif5-ID) as well as recruitment of the WRC but not Ena/VASP regulators. By contrast, deletion of Ena/VASP binding sites had strong effects on neurite retraction, with weaker phenotypes observed upon deletion of the WIRS or the Kif5-ID. Unexpectedly, removal of most of the ICD uncoupled effects on neurite retraction and synapse localization, suggesting an active role in synaptogenesis at specific intracellular locations.

RESULTS

The Fat3 ICD interacts with multiple cytoskeletal effectors

Fat3 is required for multiple features of AC development that are normally polarized (Figure 1A). In the original *Fat3* [TM] mutant (which lacks the exon encoding the transmembrane domain), ACs migrate abnormally, neurite retraction is less directed and often fails altogether, and the extra neurites form ectopic synapses in the INL and below the GCL, creating an outer and an inner misplaced plexiform layer (OMPL and IMPL, respectively) (Deans et al., 2011; Krol et al., 2016). To investigate how Fat3 mediates these diverse effects, we used mass spectrometry to identify proteins in brain lysates that bind glutathione S-transferase (GST) fusions to the Fat3-ICD; GST alone was used as a control (Avilés et

al., 2022a). Of 103 putative Fat3-ICD interactors (Table S1), Gene Ontology (GO) analysis classified many as being associated with cytoskeletal regulation (32.0%), synaptic function (11.6%), and the cell cycle (5.8%) (Figure S1A). These included known Fat3 interactors such as Kif5B, Ena/VASP family actin regulators, and the WRC component CYFIP2 (Chen et al., 2014a; Cheng et al., 2016; Krol et al., 2016; Rottner et al., 2021). In addition, we identified candidate effectors such as the microtubule binding proteins CLASP1 and CLASP2, the actin regulator Raptor, and the post-synaptic scaffold protein PSD95.

Using an overlapping series of Fat3-ICD fragments as bait for GST pull-downs, we validated the mass spectrometry results by western blot and mapped the binding sites for a subset of candidate effectors (Figures 1B; Table S2). Consistent with previous studies (Krol et al., 2016), VASP, which contains an Evh1 domain, bound to fragments containing predicted Evh1 binding sites (4, 5, 6, C) (Figure 1C). In addition, the WRC components WAVE2 and Abi1 each bound to two sites, one in the N-terminal fragments (1, 2, and N_L) and one close to the C terminus (6) (Figures 1B and 1C). Both sites contain a predicted WIRS; the first site is conserved across species (Chen et al., 2014a). Another predicted site (in fragment 3) did not bind to WAVE2 or Abi1 in our assay. These results confirm that the pull down assay detects known or predicted interactions and that short stretches of the Fat3-ICD retain physiologically relevant binding properties, consistent with the unstructured nature of the Fat3-ICD (Dosztanyi et al., 2005; Linding, 2003).We also confirmed interactions with CLASP1/2 through sites in the middle of the Fat3-ICD and with Raptor through multiple sites, as well as with PSD95 at the C terminus (Figures 1B, 1C, and S1B). Thus, the Fat3-ICD contains independent modules for recruiting proteins associated with cell morphology and neuronal development.

The developing retina differentially expresses two Fat3 isoforms

To learn how different modules in the Fat3-ICD contribute to its function, we analyzed the expression of Fat3 isoforms. Two alternative splicing events have been described: the inclusion of alternative exon 5.1 creates a 23 amino acid extension of the ECD, and the inclusion of exons 24.1 and 24.2 adds 32 amino acids to the ICD (Cheng et al., 2016) (Figures 2A and S2A; Table S3). The ICD insertion disrupts the Kif5-ID, which binds Kif5B and is important for Fat3 localization in cultured neurons (Cheng et al., 2016). To determine which of the 4 possible isoforms are expressed in the developing retina, we used nested PCR on cDNA from post-natal day 0 (P0) retinas, amplifying first a large fragment either including or excluding alternative exons followed by amplification with a second set of primers to determine whether the other splicing event also occurred (Figure S2B; Table S4). At P0, early-born ACs are elaborating dendrites in the IPL and late-born ACs are actively migrating toward the IPL, so isoforms associated with either of these developmental events should be detected. We found *Fat3* isoforms that can produce three different proteins: Fat3-ECD^{+23}ICD^{+32}, Fat3-ECD^{+0}ICD^{+32}, and Fat3-ECD^{+0}ICD^{+0} (Figure 2B).

Basescope *in situ* hybridization revealed that retinal neurons change expression of *Fat3* isoforms as they mature, as suggested by qPCR (Cheng et al., 2016). Using probes that detect the splice junction between exon (Ex) 24 and Ex25 or between Ex24.2 and Ex25 (Figures 2C and 2C′), we found that immature neurons preferentially express *Fat3* isoforms

lacking the ICD insertion (Figures 2D–2G′), whereas more mature neurons express isoforms with this insertion (Figures 2H–2K′). The *Fat3*-Ex24/Ex25 probe detected expression in the NBL throughout the period of AC birth and migration from embryonic day 14.5 (E14.5) to P0 (Figures 2D and 2E′). Expression was lower at P6, when ACs have reached their final position and are arborizing their dendrites in the IPL, and at P11, when the retina is mature (Figures 2F–2G′). At both stages, the signal was mainly in regions of the INL that house bipolar cells and ACs, with low levels in the GCL, consistent with previous reports (Deans et al., 2011; Macosko et al., 2015). In contrast, expression of the variant that contains the 96-bp insertion (detected by the *Fat3*-Ex24.2/Ex25 probe) increased as the retina matured, with low levels in the nascent INL and GCL at E14.5 that intensified as more differentiated neurons were added to the layers over post-natal development (Figures 2H–2K′). Likewise, *Fat3* isoforms with the ECD insertion were enriched in mature cells (Figure S2C). Although it is not technically possible to detect ICD and ECD insertions simultaneously, we can infer that Fat3-ECD^{+0}ICD^{+0} predominates as ACs migrate through the NBL and retract extra neurites, whereas Fat3-ECD^{+23}ICD^{+32} and Fat3-ECD^{+0}ICD^{+32} proteins are present during later stages of AC maturation and function. Thus, Fat3 may act through different intracellular signaling pathways to mediate early effects on migration and neurite retraction versus later effects on synapse formation and function.

AC migration and neurite retraction rely on different motifs in the Fat3-ICD

To learn how signaling through the Fat3-ICD contributes to its diverse effects in the developing retina, we used CRISPR-Cas9 technology to generate a series of *Fat3* mutant mouse lines (Figure 3A). To block signaling generally while preserving non-autonomous functions, we generated the *Fat3* $^{ICD-GFP}$ mouse line, where nearly the entire ICD is replaced with GFP but the ECD remains anchored to the cell membrane. As expected, the *Fat3* $^{ICD-GFP}$ allele produced a protein that is not detected by an antibody raised against Fat3-ICD, either by western blot (Figure 3B) or by immunostaining (Figures 3C and 3D); instead, western blots using a GFP antibody revealed a band of the expected size (Figure 3B). Deletion of the ICD was further confirmed by *in situ* hybridization (Figures S3A and S3B). We also generated three strains of mice lacking specific ICD motifs: the *Fat3* ^{WIRS} mouse lacks the conserved WIRS motif (MSTFHP); the *Fat3* ^{DDN} mouse line lacks amino acids DDN in the conserved Kif5-ID (D<u>DDN</u>XYH) (Cheng et al., 2016), and the *Fat3* ^{EV} mouse line lacks a 32-amino-acid stretch that contains two Evh1 binding sites (GGYDIDS<u>EYPPPHEEEFL</u>SRDQ<u>LPPPLPED</u>FP) (Figure 3A). GST pull-down from a brain lysate confirmed that binding to the expected partners was decreased without any obvious effect on binding to other cytoskeletal effectors or to PSD95 (Figures 3E and S3C–S3G). Unlike the original *Fat3* ^{TM} mutant allele, these lines are predicted to produce mutant Fat3 proteins that are inserted into the plasma membrane, consistent with their localization pattern (Figure 6).

Since young ACs preferentially express *Fat3* isoforms harboring all three motifs (Figure 2), we analyzed each mutant mouse strain for defects in AC migration, the earliest phenotype that has been described. We assessed the migration phenotype at P11 using two metrics: (1) the number of total nuclei in the IPL and (2) the number of GABAergic Bhlhb5+ nuclei in the IPL and GCL, since that AC subpopulation is the most affected in *Fat3* ^{TM}

mutants (Deans et al., 2011). In $Fat3^{ICD-GFP/ICD-GFP}$ homozygotes, AC migration was strongly disrupted, with significantly more nuclei in the IPL (10.12 ± 1.04) compared with in $Fat3^{ICD-GFP/+}$ heterozygotes (2.57 ± 0.78, $p < 0.0001$; Figures 3F, 3G, and 3N). The number of Bhlhb5^{+} ACs in the IPL and GCL was also significantly increased (15.41 ± 1.27 in $Fat3^{ICD-GFP/ICD-GFP}$ homozygotes versus 7.93 ± 0.68 in $Fat3^{ICD-GFP/+}$ heterozygotes, $p < 0.0001$; Figures 3F′, 3G′, and 3O). $Fat3^{ICD-GFP/+}$ heterozygotes also showed modest migration defects when compared with wild-type controls, suggesting that the Fat3 $^{ICD-GFP}$ protein inhibits wild-type Fat3 (Figures S3H–S3L). A similar but weaker phenotype was observed upon the deletion of the first WIRS motif and the DDN amino acids from the Kif5-ID (nuclei in the IPL: 5.16 ± 0.54 in $Fat3^{WIRS/\ TM}$ versus 0.78 ± 0.26 in $Fat3^{WIRS/+}$, $p < 0.0001$, and 2.57 ± 0.41 in $Fat3^{DDN/\ TM}$ versus 1.23 ± 0.34 in $Fat3^{DDN/+}$, $p = 0.0299$; Bhlhb5+ nuclei in IPL and GCL: 5.79 ± 0.75 in $Fat3^{WIRS/\ TM}$ versus 3.22 ± 0.33 in $Fat3^{WIRS/+}$, $p = 0.0041$, and 4.86 ± 0.68 $Fat3^{DDN/\ TM}$ versus 1.62 ± 0.43 in $Fat3^{DDN/+}$, $p = 0.0014$; Figures 3H–3K′, 3N, and 3O). By contrast, removal of the Evh1 binding sites did not affect AC migration (1.06 ± 0.23 versus 1.00 ± 0.39 nuclei in the IPL, $p = 0.5212$; 2.12 ± 0.33 versus 1.43 ± 0.36 Bhlhb5+ nuclei in the IPL and GCL, $p = 0.1692$; Figures 3L–3O). These findings indicate that Fat3 controls AC migration through a subset of motifs in its ICD, likely via interactions with Kif5B and the WRC but not Ena/VASP family members.

In $Fat3^{TM/\ TM}$ mutants, ACs show marked vacillation first of their cell bodies and then of their trailing processes (Krol et al., 2016), raising the possibility that the migration and retraction phenotypes have common molecular origins. To assess neurite retraction, we stained retinal sections for vesicular GABA transporter (VGAT), which labels GABA-containing vesicles associated with inhibitory synapses. VGAT is normally restricted to AC processes in the IPL but is mislocalized to ectopic plexiform layers in $Fat3^{TM/\ TM}$ mutants (Figures 4A and 4B), thereby indicating both the presence of extra neurites and of their synapses (Deans et al., 2011). In $Fat3^{WIRS}$, $Fat3^{DDN}$, and $Fat3^{EV}$ mutant strains, a patchy OMPL formed in short stretches of the INL at P6 (Figures 4D, 4F, and 4H). These scattered patches of ectopic synapses were largely removed by P11 (Figures S4E–S4K). By contrast, in $Fat3^{TM/\ TM}$ mutants, the OMPL is typically uninterrupted (Figure 4B) and persists until adulthood (Deans et al., 2011). The phenotypic rescue does not involve Fat1, which is also expressed in ACs, binds to Ena/VASP, and has predicted binding sites for Kif5B (Braun et al., 2007; Cheng et al., 2016; Moeller et al., 2004; Tanoue and Takeichi, 2004) (Figures S5A–S5H). Instead, it is possible that each form of mutant Fat3 retains enough activity to eliminate the extra neurites and their synapses before the retina is fully mature.

To compare the contributions of each motif, we calculated an "ectopic synapse score" for each animal. The score ranged from 0, where all sections in an animal are normal, to 1, where all sections have a strong phenotype (Figures S4A–S4D; see STAR Methods for details). In $Fat3^{TM/+}$ heterozygotes, most of the samples were normal, with rare, short stretches of OMPL (0.14 ± 0.06 ectopic synapses score), whereas $Fat3^{TM/\ TM}$ eyes exhibited an ectopic synapse score of 1 (Figures 4A, 4B, and 4I). In comparison to $Fat3^{TM/+}$ animals, $Fat3^{WIRS/\ TM}$ mutants had a significantly higher ectopic synapse score of 0.75 ± 0.03 ($p = 0.0030$; Figures 4D and 4I). A weaker effect was observed in $Fat3^{DDN/\ TM}$ mutants, with a

score of 0.46 ± 0.08 (p = 0.0122; Figures 4F and 4I). *Fat3* $^{EV/ TM}$ mutants showed signs of OMPL formation that was often quite extensive (score of 0.77 ± 0.06, p = 0.0030; Figures 4H and 4I), even in the *Fat3* $^{EV/+}$ heterozygotes (score of 0.51 ± 0.06, p = 0.0038), much as Fat3 $^{ICD–GFP}$ seems to act in a dominant negative fashion during migration (Figure S3). Notably, this variation does not parallel the variation in migration phenotypes, which were strongest in *Fat3* $^{WIRS/ TM}$ and *Fat3* $^{DDN/ TM}$ mutants and were absent from *Fat3* $^{EV/ TM}$ mutants. Thus, WRC, Kif5B, and Ena/VASP binding motifs differentially contribute to migration and neurite retraction. Although ectopic synapses also form, the presence of unretracted neurites makes it impossible to conclude whether any of these mutations directly influence synapse localization.

Genetic uncoupling of Fat3-dependent neurite retraction and synapse localization

Although we expected that synapses form secondarily to the presence of extra neurites, analysis of *Fat3* $^{ICD–GFP/ ICD–GFP}$ retinas revealed that neurite retraction and synapse localization are also controlled independently. GFP immunostaining showed localization of Fat3 $^{ICD–GFP}$ fusion protein in the IPL, in AC cell bodies, and also in the tips of neurites pointing away from the IPL. These extra neurites were significantly more abundant in *Fat3* $^{ICD–GFP/ ICD–GFP}$ mice (25.85 ± 1.96 GFP+ ectopic neurites per field of view at P6 and 20.63 ± 2.68 at P11) than in *Fat3* $^{ICD–GFP/+}$ controls (15.67 ± 2.39 at P6 and 6.83 ± 0.89 at P11, p = 0.0030 and 0.0002; Figures 5A–5E). However, despite the presence of many unretracted neurites, no ectopic VGAT+ synapses were observed at any age (Figures 5H, 5K, and S6C), in sharp contrast to what occurs in *Fat3* $^{TM/ TM}$ mice (Deans et al., 2011) and other *Fat3* mutant strains (Figure 4). To the contrary, synapse development was inhibited, with a significant decrease in VGAT staining intensity in the IPL at P6 (2.97 ± 0.07 units of normalized VGAT mean fluorescence in homozygotes versus 3.75 ± 0.08 units in wild type [WT], p < 0.001, Mann-Whitney test) (Figures 5F, 5H, and 5L) and at P11 (2.66 ± 0.10 in *Fat3* $^{ICD–GFP/ ICD–GFP}$ and 3.54 ± 0.06 units in WT, p < 0.0001, t test) (Figures 5I–5K, and 5M). At P11, levels of the inhibitory post-synaptic protein Gephyrin were also reduced, confirming that synapse development was disrupted (1.84 ± 0.04 units in WT, 1.61 ± 0.05 units in *Fat3* $^{ICD–GFP/+}$, and 1.68 ± 0.05 units in *Fat3* $^{ICD–GFP/ ICD–GFP}$; p = 0.0007 for *Fat3* $^{ICD–GFP/+}$ and p = 0.0290 for *Fat3* $^{ICD–GFP/ ICD–GFP}$, Mann Whitney test) (Figures 5I′–5K′, and 5M). Similar to the dominant effect of the *Fat3* ^{EV} protein on neurite retraction, VGAT levels in the IPL of *Fat3* $^{ICD–GFP/+}$ heterozygotes were affected at both ages (3.24 ± 0.08 units in *Fat3* $^{ICD–GFP/+}$ heterozygotes, P6, and 2.73 ± 0.11 in *Fat3* $^{ICD–GFP/+}$, P11; p = 0.0001 for each versus WT; Figures 5F, 5G, 5I, 5J, 5L, and 5M). By P22, the phenotype was corrected (Figures S6A–S6D). Thus, whereas ectopic synapses form when Fat3 is absent from the cell surface (as in *Fat3* ^{TM}), expression of a membrane-anchored ECD (as in *Fat3* $^{ICD–GFP}$) had the opposite effect. This surprising observation suggests that while neurites may form synapses opportunistically in some contexts, Fat3 can also affect synapse development directly.

We wondered whether the differing effects on synapse development might correlate with the localization of the mutant forms of Fat3, such that the presence of Fat3 $^{ICD–GFP}$ at the tips of the ectopic neurites might actively inhibit synapse development here as in the IPL. To visualize Fat3 ^{WIRS}, Fat3 ^{DDN}, and Fat3 ^{EV} protein localization, we crossed each strain to

the *Fat3* [TM] allele and stained with an antibody to the Fat3-ICD. No signal was detected in the IPL of *Fat3* [TM/ TM] retinas, confirming that any signal in *Fat3* [TM] heterozygotes comes from the other *Fat3* allele (Figures 6A and 6B). In *Fat3* [WIRS/ TM], *Fat3* [DDN/ TM], and *Fat3* [EV/ TM] mutants, Fat3 protein was detected both in the IPL and also ectopically in the INL (Figures 6D, 6F, and 6H). Thus, *Fat3* [ICD−GFP]'s inhibitory effects on synapse development more likely relate to the absence of the ICD rather than to its mislocalization to processes outside of the IPL. Of note, even in the rare cases where ectopic neurites were observed in *Fat3* [TM/+] heterozygotes, visualized by VGAT staining, no significant Fat3 protein was detected in the OMPL (Figure 6C). This suggests that Fat3 mislocalization is not secondary to the presence of the neurites and that all three motifs are required for proper localization.

The WRC is required for AC migration

If the Fat3-ICD acts through distinct motifs to recruit effectors for Fat3 localization, migration, neurite retraction, and synapse formation, then the deletion of a putative effector should elicit the same phenotype as the deletion of its binding site. To test this idea, we focused on the WRC, which shapes the actin cytoskeleton locally upon binding to the WIRS motif in cell surface receptors (Chen et al., 2014a) and has known effects on neuronal migration (Fan et al., 2018; Grove et al., 2004). Indeed, ACs express many WRC components, including Abi1 and Abi2 (Figure S7), WAVE2, CYFIP2, Nap1 (*Nckap1*), and BRICK1 (*Brk1*) (Macosko et al., 2015; Yan et al., 2020). Given the strong migration phenotype in *Fat3* [WIRS] mutants, we hypothesized that Fat3 controls directed migration by localizing the WRC to processes directed toward the IPL. To test this idea, we compared Abi1/2 distribution in control and *Fat3* [TM/ TM] eyes at E16.5, when early-born ACs are migrating through the NBL. In control eyes, Abi1/2 was enriched in leading processes in the proto-IPL (Figure 7A). In *Fat3* [TM/ TM] eyes, Abi1/2 staining was more intense throughout the retina, including in migrating cells (Figures 7A and 7B). Later, at P0, Abi1/2 proteins were ectopically localized to the extra neurites that form in *Fat3* [TM/ TM] ACs (Figures 7C–7E). This suggests that Fat3 normally restricts the WRC to processes pointing toward the developing IPL.

We tested whether the WRC is required for AC migration by deleting *Abi1*, which is critical for WRC function (Dubielecka et al., 2011). To circumvent lethality, we generated a conditional knockout (cKO) using a proven floxed *Abi1* mouse line (Dubielecka et al., 2011) together with *Six3*[CRE], which is active throughout the retina starting at E9.5 (Ray et al., 2018). Loss of *Abi1* from the retina was confirmed by *in situ* hybridization and western blot (Figures S7A–S7D). The overall structure of the retina was largely normal in *Abi1* cKOs (*Six3*[CRE/+];*Abi1*^{fl/fl}). However, AC migration was disrupted, with significant effects on the number of nuclei in the IPL (3.00 ± 0.59 nuclei in the IPL per field in *Abi1* cKOs versus 1.00 ± 0.56 in *Six3*[CRE/+];*Abi1*^{fl/+} controls, p = 0.0183) and of Bhlhb5+ nuclei in the IPL and GCL (8.42 ± 0.62 in *Abi1* cKOs versus 5.75 ± 0.63 in *Six3*[CRE/+];*Abi1*^{fl/+}, p = 0.0063; Figures 7F–7I). Although *Fat3* [WIRS/ TM] mutant retinas develop ectopic synapses, we did not observe any change in VGAT localization in P6 *Abi1* cKOs (Figures 7J and 7K), nor was there a change in VGAT intensity in the IPL (2.87 ± 0.17 versus 2.75 ± 0.08 units in *Six3*[CRE/+];*Abi1*^{fl/+}, p = 0.7289; Figures 7J–7L). Since Abi2 protein persists

(Figures S7E–S7G), it is possible that later effects of Fat3-WRC interactions are masked in *Abi1 cKOs*. Taken together, these results show that Fat3/WRC interactions are crucial for neuronal migration and emphasize the independent contributions of different effectors to Fat3's effects on migration, neurite retraction, and synapse development.

DISCUSSION

To form circuits that are organized for the directed flow of information, neurons must migrate to the correct position, extend neurites to find synaptic partners, and then send the machinery needed to make synapses to that location. Here, we show that Fat3 functions as a molecular node to coordinate these polarization events among retinal ACs throughout development, echoing the classic role of tissue polarity proteins in epithelial structures. We find that Fat3 achieves functional versatility by recruiting diverse cytoskeletal regulators and synaptic proteins that bind to discrete regions of the ICD, with different sets of motifs influencing AC migration, neurite retraction, and synapse localization (Figure 7M). Since Fat3 is asymmetrically localized to AC neurites, so are its effectors, creating an efficient system for inducing intracellular asymmetries that are globally oriented across the population even as developmental needs evolve. Indeed, even after the ACs acquire their morphologies, this system seems to act independently to bias where their synapses form. As the ACs mature, the composition of the Fat3-ICD and -ECD changes, adding an additional layer of flexibility. These findings suggest a molecular explanation for how developing neurons orchestrate multiple polarized cell biological events that are properly oriented with respect to the nervous system.

Although defects in neuronal migration early in retinal development can have secondary effects on cell morphogenesis (Rocha-Martins et al., 2021) or synapse localization (Collin et al., 2020), we find that Fat3 acts through effectors that independently contribute to each of these important steps in AC development. For instance, a WIRS motif binds the WRC, which induces actin filament branching, whereas the Evh1 binding sites recruit Ena/VASP proteins, which promote actin filament elongation (Bear and Gertler, 2009; Rottner et al., 2021). Although these are all actin regulators, deletion of the WIRS disrupts migration whereas deletion of the Evh1 binding sites does not (Figure 3). On the other hand, deletion of the Evh1 binding sites had stronger effects on neurite retraction than did deletion of the WIRS. Additionally, Fat3's effects are not limited to the actin cytoskeleton but may also depend on Kinesin-1, which is a motor that moves cargo toward the plusend of microtubules(Hirokawaetal., 2009) (Figure 4). The binding sites act independently, as evidenced by the binding properties of small portions of the ICD and by the selective loss of predicted binding partners upon deletion of each motif (Figures 1 and 3). Modularity is further illustrated by alternative splicing, which changes the composition of the ICD during development. Thus, Fat3 can shape the cytoskeleton in slightly different ways during migration, when the WRC plays a prominent role, than during neurite retraction, when localization of Ena/VASP proteins seems to be key. This mechanism preserves the overall polarity of retinal circuits, even as more cells and synapses are added.

Like other tissue polarity proteins, Fat3 appears to induce cellular asymmetries by localizing cytoskeletal regulators. Although previously inferred for Fat3-Ena/VASP interactions (Krol

et al., 2016), our data suggest that this is a key feature of Fat3 activity. For instance, we find that Fat3 binds to the WRC components Abi1 and WAVE2 and that asymmetric localization of Abi1/2 in the IPL is lost in *Fat3* [TM] mutants (Figures 1 and 7). Moreover, deletion either of the juxtamembrane WIRS or of *Abi1* caused an AC migration phenotype (Figures 3 and 7), consistent with recent findings showing that loss of *Cyfip2* affects AC migration (Chaya et al., 2021). Notably, this role is conserved, as *Drosophila* Fat-like also contains two WIRS motifs and localizes the WRC to cell contacts during collective cell migration (Squarr et al., 2016). However, other effectors likely contribute, since *Fat3* [ICD–GFP] mutants exhibit a migration phenotype that is stronger than in *Fat3* [WIRS] or *Fat3* [DDN] mutants (Figure 3). This might be due to the presence of a second WIRS motif or the incomplete abrogation of binding to Kif5B; some of the other Fat3 binding proteins that we identified might also contribute (Table S1).

Although one of Fat3's core functions is to localize effectors, the ultimate outcome differs depending on which effectors are recruited. Thus, while the WRC seems to be a major player for AC migration, neurite retraction depends more heavily on Ena/VASP proteins. As for the WRC, this phenotype likely depends on asymmetric protein localization, since deletion of the Evh1 binding sites in the Fat3-ICD impacted neurite retraction (Figure 4) and a similar phenotype is caused upon the redistribution of Ena/VASP proteins (Krol et al., 2016). In this case, Ena/VASP proteins may cooperate with other effectors. For instance, Ena/VASP proteins can bind to Abi1 and hence enhance WRC activation to influence cell morphology (Chen et al., 2014b) and induce dendrite retraction in worms (Sundararajan et al., 2019). Indeed, neurite retraction is also disrupted in *Fat3* [WIRS] mutants (Figure 4). Effectors such as CLASP1/2 and Raptor could also be involved, given their reported effects on neurite development (Lee et al., 2004; Urwyler et al., 2019). Additionally, CLASP genetically interacts with *fat-like* in *Drosophila* egg chamber development (Chen et al., 2016).

While WRC and Ena/VASP proteins may confer specific outcomes, other binding partners may influence Fat3 activity more generally by ensuring its asymmetric distribution. For instance, the motor protein Kif5B is important for localizing Fat3 to the distal neurites of hippocampal neurons (Cheng et al., 2016) and could play a similar role in ACs. Consistent with this idea, immature retinal neurons predominantly express a Fat3 isoform with a Kif5-ID (Figure 2), and Fat3 [DDN] accumulates ectopically in ACs, with accompanying defects in both migration and neurite retraction (Figures 3, 4, and 6). Later in development, other mechanisms may take over, since Fat3 isoforms in mature neurons rarely contain the Kif5-ID, and Fat3 [WIRS] and Fat3 [EV] proteins also show altered localization (Figures 2 and 6). Indeed, in flies, asymmetric localization of Fat-like is proposed to initiate early microtubule polarization that is amplified and reinforced by other effectors (Chen et al., 2016; Viktorinová and Dahmann, 2013). ECD-mediated interactions may also contribute, since all of the mutant forms of Fat3 also traffic to its normal location in the IPL (Figure 6).

An unexpected outcome of this work was the realization that Fat3 may actively promote the formation of localized synapses. Previously, we observed that ectopic synapses form when there is no Fat3 at the cell surface (Deans et al., 2011), a phenotype that could be secondary to the retention of extra neurites. However, we find instead that these two phenotypes

can be separated, since no ectopic synapses form in *Fat3* [ICD–GFP] mutants, despite the presence of many extra neurites (Figure 5). Ectopic synapses form in the other mutant strains. Although it is possible that each of these mutant strains has lost Fat3's ability to localize synaptic proteins to the IPL, this is difficult to reconcile with the strong antagonistic effect of Fat3 [ICD–GFP], which lacks all of the same motifs. Since the mutant proteins all localize to the unretracted neurites, an alternative explanation is that Fat3 [DDN], Fat3 [WIRS], and Fat3 [EV] proteins engage with their natural ligands and thus localize effectors that promote synapse development at that site, in this case through motifs unaffected by each of the mutations. By contrast, with essentially no ICD, Fat3 [ICD–GFP] is unable to recruit the necessary effectors, so even upon ligand binding, synapses fail to form. Several synapse-related proteins bind to the Fat3-ICD and could be involved, such as PSD95, which can still bind to Fat3 [DDN], Fat3 [WIRS], and Fat3 [EV] proteins (Figure 3). The WRC could also contribute, given its known importance for synapse formation (Chia et al., 2014). However, ectopic synapses still form in *Fat3* [WIRS] mutants, possibly due to the retention of the second WIRS motif or to the ability of other Fat3 binding partners to recruit the WRC. The specific contributions of the WRC remain unclear, as there were no obvious synaptic phenotypes in *Abi1 cKO* retinas, perhaps due to compensation by Abi2 (Figures 7 and S7).

Our data also highlight a role for the Fat3-ECD during synapse development. For instance, the presence of even one copy of the Fat3-ECD is inhibitory, as evidenced by the *Fat3* [ICD–GFP] phenotype in the IPL (Figure 5). This dominant negative effect, which is also seen in AC migration (Figure S3), may be caused by *cis* interactions between WT and mutant proteins, as have been observed to occur among other Fat-related proteins (Badouel et al., 2015). Notably, during synaptogenesis, ACs produce a form of Fat3 with an insertion in its ECD that could alter ligand binding and thus further diversify Fat3's effects on AC development, maturation, and function (Figure S2). The ECD may also mediate Fat3's ability to distinguish appropriate targets in the IPL from those in ectopic locations, where the ligand may be available only in other mutant ACs that also have unretracted neurites. This might explain both why the OMPL is patchy and why an IMPL does not form in *Fat3* [DDN], *Fat3* [WIRS], or *Fat3* [EV] mutants. The identification of the relevant ligand(s) is an important next step.

Our results favor a model where Fat3 determines where synapses will be, not whether they form. Thus, synapses form in the absence of Fat3, just in the wrong location, perhaps because Fat3 is not present to corral the relevant molecules. On the other hand, when Fat3 is present but mislocalized, so are the synapses, as long as the ICD is present. Although contradictory at first glance, these results fit with observations from *Drosophila*, where DIP proteins influence synaptic partner preference but not formation of synapses per se (Xu et al., 2019). Indeed, DIP mutant phenotypes are qualitatively similar to what occurs in *Fat3* mutants, with synapses apparently forming promiscuously at sites of cell-cell contact. One possibility is that Fat3 localizes other receptors that provide specificity, much as Fat proteins localize DCC for directed migration in worms (Sundararajan et al., 2014). Indeed, several other adhesion systems are necessary for proper synapse localization (Matsuoka et al., 2011a, 2011b; Ray et al., 2018) and could cooperate with Fat3 in the developing IPL. Given the rich array of putative binding partners and Fat3's proven versatility, it is possible

that Fat3 influences many other features of synapse development and function that remain to be discovered.

Limitations of the study

Our results suggest that Fat3 interacts with different sets of effectors to elicit a variety of asymmetric cell behaviors, with clear evidence that Fat3-WRC interactions are essential for neuronal migration. However, the view remains incomplete, as we have confirmed only a subset of interactions, both biochemically and genetically. For instance, due to the need for abundant material, we performed the mass spectrometry analysis using protein lysates from the brain rather than from the retina. Thus, some of the binding partners that we found may not be relevant to retinal development, and, conversely, additional partners may have been missed. Along the same lines, some of the mutations we made may not completely block effector recruitment. For instance, we removed only the first WIRS motif from the Fat3-ICD, which was selected based on its conservation across species and its binding strength. However, the WIRS site at the C terminus of Fat3-ICD may be able to recruit enough WRC to mediate a subset of Fat3's activities, and Abi2 may compensate for Abi1 in some contexts. Additional roles for Fat3-WRC interactions may be discovered upon the deletion of both WIRS sequences from the Fat3-ICD or the analysis of *Abi1/2* double KOs. Additionally, although *Fat3* isoform expression switches during retinal development, it remains unclear which cells express which isoforms and how each isoform influences retinal development. For instance, the Basescope method does not permit us to detect the ECD and ICD insertions simultaneously. It is also important to point out that nothing is known about the role for Fat3 in other retinal cell types or how this might influence AC development. Finally, while our data suggest that Fat3 can directly impact synapse formation, we can only speculate about how this might work without knowing more about the role of the ECD and its ability to engage with other proteins, both in *cis* and in *trans*. With a more complete picture of Fat3's signaling properties, we will be in a better position to understand the puzzling range of synaptic phenotypes that we have observed.

STAR★METHODS

RESOURCE AVAILABILITY

Lead contact—Further information and requests for resources and reagents should be directed to and will be fulfilled by the Lead Contact, Lisa V. Goodrich (Lisa_Goodrich@hms.harvard.edu).

Materials availability—All unique reagents generated in this study are available from the Lead Contact without restriction. Plasmids and mouse strains (whenever available in our colony) will be shared with reasonable compensation by requestor for shipping. Some of the mouse strains generated in this study will be available as cryopreserved sperm at Charles River Laboratories, Wilmington, MA, USA.

Data and code availability

- Mass spectrometry data and source data have been deposited at Harvard Dataverse (Avilés et al., 2022a, 2022b) and are publicly available as of the date of publication. DOIs are listed in the key resources table.

- This paper does not report original code.

- Any additional information required to reanalyze the data reported in this paper is available from the lead contact upon request.

EXPERIMENTAL MODEL AND SUBJECT DETAILS

Animals—Transgenic mice expressing Cre recombinase were obtained from the following sources: *Six3*^CRE (Jackson lab, 019755) (Furuta et al., 2000), *Ptf1a*^CRE (C. Wright, Vanderbilt U.) (Fujitani et al., 2006). Floxed alleles for *Abi1* and *Fat1* were kindly provided by Dr. L. Kotula (SUNY Upstate Medical University) (Dubielecka et al., 2011) and Dr. F. Helmbacher (Institut de Biologie Du Développement de Marseille) (Caruso et al., 2013), respectively. *Fat3* ^™ (a.k.a. KO or *Fat3*^−/−) mutants were described previously (Deans et al., 2011). All mutant mice generated in this study are described below. For timed pregnancies, noon on the day of the plug was considered embryonic day 0.5 (E0.5). Embryos and pups of either sex were used. Mice were maintained on a 12 h/12 h light/dark cycle at 18–23°C and 40–60% humidity. Animals were handled ethically according to protocols approved by the Institutional Animal Care and Use Committee at Harvard Medical School.

Cell lines—HEK293 cells were kindly provided by Michael Greenberg's laboratory at Harvard Medical School.

METHOD DETAILS

Generation of mutant alleles—To generate the *Fat3* ^ICD–GFP allele, J1 ES cells were electroporated with a plasmid containing the CRISPR guide RNA and the *Cas9* gene, together with a plasmid containing a sequence for homology repair. The guide RNA targets a sequence that codes for the 5′ end of the *Fat3* ICD (TAATCGTACTCTTCATCGTC) and the repair plasmid contains homology arms flanking a region that codes for 10 juxtamembrane amino acids (RKKVFRKNYS) followed by GFP, the WRPE sequence, and a SV40 polyA. ES cell clones were screened and sequenced using primers that flanked the inserted region to confirm the presence of the mutation in the correct location. After confirming the correct karyotype, ES cell clones were injected into blastocysts of C57Bl6/J pregnant females in the Transgenic Core Facility (Brigham and Women's Hospital, Harvard Medical School, Boston, MA). The resulting chimeras were screened by percentage of agouti coat color and were further crossed to C57Bl6/J mice. Agouti progeny were genotyped and heterozygotes used as founders.

To generate the *Fat3* ^WIRS allele, we deleted the first WIRS site (MSTFHP) by CRISPR/Cas9 technology. After testing for efficiency *in vitro*, an RNA-based guide RNA (Synthego) was directly injected into zygotes of C57Bl6/J pregnant females together with a single-stranded-based DNA donor sequence (IDT) and the Cas9 protein (IDT, Cat#1081058) in the Genome Modification Facility (Harvard University, Cambridge, MA). The guide

RNA targeted the sequence GAATCTCCACGCATCCTGAC in the *Fat3* gene and the repair donor was a 593 bp fragment that contained homology arms (bp 580022–580353 and 580371–580632 in NCBI: NC_000075.6) but lacked the sequence for the WIRS site (ATGAGCACATTCCACCCA). The resulting mice were screened by genotyping around the area where we expected the mutation and the PCR was run on a polyacrylamide gel to detect short deletions. A fragment flanking the homology-directed repair (HDR) donor was amplified from positive samples, cloned into a TOPO vector, and sequenced to corroborate the mutation and the integrity of the regions around the junctions of the HDR donor.

Fat3 ^{DDN} mice were generated using a guide RNA that targets the sequence TCAGACTCTGGAGATGACAA located in *Fat3* exon 24 adjacent to the splice donor and catalyzes a DNA break within sequences encoding the Kif5B interacting domain. This targeting strategy was developed by the University of Utah Mutation Generation and Detection Core. The guide RNA was co-injected with a *Cas9* expression plasmid into CBA/C57Bl6 F1 pronuclei that were subsequently implanted into pseudo pregnant-females by the University of Utah Transgenic and Gene Targeting Core. Mouse pups were genotyped by PCR amplification of tail DNA using primers flanking the predicted cut site, and amplified DNA was cloned into a TOPO vector for DNA sequencing to determine the nature of the deletion. A single male mouse with a 9 base pair deletion resulted in the *Fat3* ^{DDN} mutation. This internal deletion was selected because it disrupted the Kif5B interaction domain without causing a frame shift or impacting the splice donor sequence at the 3′ end of exon 24.

To generate the *Fat3* ^{EV} allele, oocyte injections were performed with RNA encoding the Cas9 enzyme (Trilink) as well as guide RNAs targeting Cas9 nuclease to two sites in the *Fat3* locus, one just C terminal, and one just N terminal of the Ena/VASP binding site. The injections were done by the Transgenic Mouse Facility (Brigham and Women's Hospital, Boston, MA). The guide RNAs were encoded in the pX330 vector and their target sequences were: GAGAGTGACTACTACCTAGG and GGACTTCCCTGACCAGTATG. The guide RNAs were validated by transfection of 3T3 cells and screening with the Surveyor Assay Kit. To create an in-frame and engineered deletion of the Ena/VASP binding site, a template repair oligonucleotide (IDT) was also injected. The presence of the mutation was confirmed by PCR genotyping and sequencing of the locus.

All lines were maintained on the C57Bl/6 background and evaluated for mutant phenotypes by intercrossing with the *Fat3* ^{TM} allele to control against off-target phenotypes.

GST Pull down, mass spectrometry, and Western blot—To identify intracellular binding partners of Fat3, we generated a Fat3-ICD construct fused to Glutathione-S-transferase (GST) and GST alone, as a control, by expression of a pGEX6P-1-GST backbone plasmid in Rosetta *E. coli* (Millipore). After 4 h (h) of IPTG induction, bacteria were harvested and pellets were lysed in PBS with 1% Triton X-100, 1mM EDTA, and 0.1mg/ml lysozyme supplemented with 1mM Pefabloc SC PLUS protease inhibitor (Roche, Rochester, NY) and 1mM DTT. Fusion proteins in bacterial lysate were bound to glutathione sepharose beads (GE Life Sciences) in batch, approximately 50µl of beads/construct for 4 h at 4°C. Beads were washed 2x in PBS/0.5% Triton X-100 supplemented with 1mM

DTT and 1x in PBS/1mM DTT. Beads were snap frozen in PBS/25% glycerol/1mM DTT and stored at −80°C. To make brain lysates, a P1 mouse brain was dissected and dounce homogenized on ice with 750 μl lysis buffer and incubated on ice for 30 minutes. Homogenate was spun at 10, 000 × g for 30 minutes (min). A volume of 900 μl of lysate was added to 50 μl of beads bound to fusion protein and rotated at 4°C overnight. Beads were spun at 600 g for 3 min, unbound brain lysate supernatant was collected, and beads were washed 5x with 400 μl PBS/DTT, with 10 min in between spins. A volume of 50 μl of beads was combined with 45 μl lysis buffer and 25 μl 4x NuPage sample buffer (Invitrogen). Following pulldown, brain lysate input, supernatant and beads were analyzed by standard Western blot. For mass spectrometry analysis, beads were run out on a Tris –Glycine polyacrylamide gel, bands cut, trypsin digested and analyzed by the Children's Hospital IDDRC proteomics core. The list of candidate Fat3-ICD interactors yielded by mass spectrometry was filtered for proteins that were found in the GST alone condition, background contaminants (found in the CRAPome), and viral proteins. To map binding sites in Fat3-ICD, we constructed several fragments of Fat3-ICD fused to GST (Table S2). These GST-fusion fragments were generated and used to pulldown proteins form brain lysates as described above.

To validate the binding of *Fat3* mutant alleles, we generated Fat3-ICD constructs using the pCMV-GST backbone plasmid (Tsai and Reed, 1997) as follows: Fat3-ICD[WT], Fat3-ICD [WIRS], Fat3-ICD [DDN] and Fat3-ICD [EV]. The plasmids were transfected into HEK293 cells using Lipofectamine (Invitrogen, see manufacturer's recommendations for details) and fusion proteins were collected after 2 days by scraping the cells with lysis buffer and centrifugation at $16,000 \times g$ for 15 min. Glutathione Sepharose 4B (50% slurry) was combined with protein lysates and incubated at 4°C for 3 h. after several washes with PBS/ 0.5% Triton X-100/1mM DTT and PBS/1mM DTT, the beads were collected and incubated with protein lysates from a P1 mouse brain at 4°C overnight. After centrifugation, the supernatant was collected and following several washes with PBS/1mM DTT, the beads were resuspended in 1x XT sample buffer (BioRad).

For Western blots, samples were denatured at 95°C for 10 mins and subjected to SDS-PAGE in a 4–12% Criterion™ XT Bis-Tris Protein Gel (Bio-Rad) using XT MES Running Buffer (Bio-Rad). After 2 h at 150 V of electrophoresis, the proteins were transferred to Immobilon-P PVSF (0.45 μm, Sigma-Millipore) in Tris-Glycine buffer supplemented with 20% methanol for 1 h at 75 V. The Immobilon-P membranes were blocked with 5% skim milk in TBS buffer and then incubated with primary antibodies at 4°C overnight. The primary antibodies used for Western blots were: mouse anti-Abi1 (1:500, MBL, Cat#D147–3), rat anti-CLASP1 (1:500, Absea, Cat#050801A06), rat anti-CLASP2 (1:500, Absea, Cat#032012H02), goat anti-GFP-FITC (1:500, Abcam, Cat#ab6662), rabbit anti-GST (1:10,000; Cell Signaling, Cat#2625S), goat anti-Kif5fB (1:500, Imgenex, Cat#IMG-3049), rabbit anti-PSD95 (1:1,000; Abcam, Cat#ab18258), rabbit anti-Raptor (1:1,000; Cell Signaling Cat#2280), rabbit anti-VASP (1:2,000; kind gift from Dr. Frank Gertler, MIT) and rabbit anti-WAVE2 (1:325, Cell Signaling, Cat# 3659). After several washes with TBS supplemented with 0.5% Tween 20 (Sigma-Aldrich), the membranes were incubated with secondary HRP-conjugated antibodies diluted 1:2,000 for 1–2 h at room temperature.

The signals were developed by using Clarity ECL substrate following the manufacturer's instructions (Bio-Rad). Western blots were done at least twice with similar results.

Dissections and immunohistochemistry—To obtain retinal tissue, animals of the desired postnatal age were euthanized by CO_2 inhalation and cervical dislocation. Extraocular tissue, the cornea and the lens were removed from the eyes and the eyecups were further fixed by immersion in 4% paraformaldehyde (PFA, EMS Cat#15710) for 30 min at room temperature or 15 min on ice for anti-Gephyrin staining. After several washes with Sorenson's buffer, the eyes were submerged in 30% sucrose and kept at 4°C for at least 2 h. Embryonic eyes were obtained by euthanizing the pregnant females and fixing the whole embryo head in 4% PFA overnight at 4°C. Then, the heads were cryoprotected sequentially in 10% and 30% sucrose until the heads sunk. After sucrose cryoprotection, either eyes or heads were incubated in NEG-50 (VWR, Cat#84000–154) overnight at 4°C and embedded by freezing in a liquid nitrogen vapor bath. Retinal slices were obtained by cryosectioning the eyes or embryonic heads (coronal orientation) at 20 μm thickness and mounting on Superfrost® Plus Micro Slide (VWR, Cat#48311–703). The sections were either stained immediately or stored at –80°C.

For immunohistochemistry, NEG-50 was removed by short incubation in PBS and then sections were blocked and permeabilized by incubation in 5% Normal Donkey Serum (NDS, Jackson ImmunoResearch Cat#017-000-121) in Sorenson's supplemented with 0.5% Triton-X for 1–2 h at room temperature. Sections were then incubated in primary antibody diluted in blocking buffer overnight at 4°C. After several washes with PBS, sections were incubated with fluorescent secondary antibodies diluted in 5% NDS in Sorenson's supplemented with 0.02% Triton-X for 1.5–2 h at room temperature. After final washes, sections were mounted in DAPI-Fluoromount-G (SouthernBiotech Cat#0100–20). Primary antibodies used for immunohistochemistry were: mouse anti-Abi1/2 (1:300; Thermo Fisher Scientific Cat#PA5–78705), goat anti-Bhlhb5 (1:500; Santa Cruz, Cat#sc-6045), mouse or rabbit anti-Fat3 (Deans et al., 2011), mouse anti-Gephyrin (1:100, Synaptic Systems, Cat#147 011), chicken anti-GFP (1:500; Aves, Cat#GFP-1020), rabbit anti-Pax6 (1:400; Biolegend, Cat#901301), and rabbit anti-VGAT (1:300; SynapticSystems, Cat#131002). All secondary antibodies were diluted 1:1,000 and were: Donkey anti-chicken Alexa Fluor® 488, Goat anti-chicken Alexa Fluor® 488, Donkey anti-goat Alexa Fluor® 568, Donkey anti-mouse Alexa Fluor® 488, Donkey anti-mouse Alexa Fluor® 568, Goat anti-mouse Alexa Fluor® 647, Donkey anti-rabbit Alexa Fluor® 488, Donkey anti-rabbit Alexa Fluor® 568 and Donkey anti-rabbit Alexa Fluor® 647.

***In situ* hybridization (RNAscope and basescope)**—Tissue collection was performed similar as to for immunohistochemistry, except using RNAase-free conditions. For RNAscope *in situ* hybridization, we used RNAscope® Fluorescent Multiplex Reagent Kit (ACD, Cat#320850) or RNAscope® Fluorescent Multiplex Reagent Kit v2 (ACD, Cat#323120) assays following the manufacturer's instructions. In brief, retinal sections were post-fixed in 4% PFA for 15 min at room temperature, treated with hydrogen peroxide for 10 min at room temperature (only v2 assay) and treated with Protease III for 10 min at 40°C before probe incubation. Probes were obtained from ACD (see

key resource table). If immunohistochemistry was performed after *in situ* hybridization, sections were rinsed in PBS after the final RNAscope wash and permeabilized and blocked again with 5% NDS/0.5% Triton X-100 Sorenson's buffer, followed by the regular immunohistochemistry protocol. To detect specific isoforms, we used Basescope™ Detection Reagent Kit – RED assay (ACD, Cat#322900), following the manufacturer's instructions and pretreating the retinal sections with post-fixation in 4% PFA for 15 min at room temperature, incubation with hydrogen peroxide for 10 min at room temperature and treatment with Protease III for 10 min at 40°C before probe incubation. Basescope probes were obtained from ACD (key resources table). Basescope probe *Fat3*-Ex24Ex25 (a.k.a BA-Mm-Fat3-E24E25) spans the junction of exons 24 and 25 (nucleotides 13006–13051 in GenBank: NM_001080814.1). Basescope probe *Fat3*-Ex24.2Ex25 (a.k.a. BA-Mm-Fat3-x1-E25E26) spans the junction of exons 24.2 and 25 (nucleotides 14180–14226 in GenBank: XM_011242543.2). Basescope probe *Fat3*-Ex5Ex6 (a.k.a. BA-Mm-Fat3-E5E6) spans the junction of exons 5 and 6 (nucleotides 4155–4195 in GenBank: NM_001080814.1) and Basescope probe *Fat3*-Ex5.1Ex6 (a.k.a. BA-Mm-Fat3-x1-E6E7) spans the junction of exons 5.1 and 6 (nucleotides 5235–5276 in GenBank: XM_011242543.2).

Image acquisition—After immunostaining, RNAscope or Basescope, retinal sections were imaged within 300 μm from the optic nerve head on a Leica SP8 confocal microscope. The entire sections were imaged in consecutive z-slices separated by 1 μm using a 40x or 63x oil objective. The z stacks were then projected at maximum fluorescence intensity using Fiji/ImageJ.

RT-PCR—Eyes from P0 wild type mice were dissected as described above under RNAse free conditions. A pool of 6 retinas (from 3 mice) were separated from the sclera, RPE and optic nerves, and then homogenized in TRIzol reagent (Thermo Fisher Scientific, Cat# 15596026). Total RNA was further extracted with chloroform and precipitated with isopropanol. For reverse transcription, a total of 1 μg of RNA was combined with 250 ng of random primers (Thermo Fisher Scientific, Cat#48190011), 10mM of dNTP mix, 1x First-Strand buffer, 5mM DTT 40 units of RNaseOUT (Thermo Fisher Scientific, Cat#10777019) and 200 units of SuperScript III RT (Thermo Fisher Scientific, Cat#18080044). The reaction mix was incubated at 50°C for 1 h and inactivated at 70°C for 15 min. The resulting cDNA served as template in PCR reactions using PfuUltra II Fusion High-fidelity DNA Polymerase (Agilent, Cat# 600674) following the manufacturer's instructions and PCR cycles (35–40 cycles) of 20 seconds (s) at 95°C, 20 s at 50–55°C (lower T_m of primer − 5°C) and 30 s/1kb at 72°C (see Table S3 for details of each reaction). To determine which isoforms are expressed in P0 retinas, we performed nested PCR, where a ~9 kb fragment was amplified from P0 retinal cDNA (see Table S4 for details), gel purified, and used as a template to detect either the extracellular or intracellular insertions. To detect the extracellular insertion, we used primers EA41 and EA67, which generate a product that spans exons 4, 5, 5.1 (if present), 6 and 7. Half of the reaction was digested with the restriction enzyme *Xho*I (New England BioLabs Cat# R0146), for which exon 5.1 has a target site (see Table S3 for details). To detect the extracellular insertion, we used primers EA99 and EA100, which generate a product that spans exons 23, 24, 24.1/24.2 (if present) and 25. Half of the reaction

was digested with the restriction enzyme *Nsi*I (New England BioLabs Cat# R3127), for which exon 5.1 has a target site (see Table S3 for details).

External gene expression profile datasets used for consultation—Expression of WRC components in the retina was analyzed using the single-cell RNAseq portal from the Broad Institute (MIT and Harvard, Cambridge, MA). https://singlecell.broadinstitute.org/single_cell. Study SCP301 and SCP919.

QUANTIFICATION AND STATISTICAL ANALYSIS

All quantifications were done blind to condition by assigning random numbers to each image. Only after the quantification was done, the identity of the images was revealed to assign the values to their corresponding condition. For each type of quantification, a pilot experiment was done to determine the appropriate number of animals and/or samples that would be needed. All the procedures were done under the same technical conditions and when the intensity of fluorescence was measured, all the parameters where kept constant between control and experimental conditions. The animal (N) and sample (i.e. sections, n) numbers, statistical test performed, and *p* values are indicated in figure legends and/or figures.

To assess AC migration, we quantified the number of cells (as indicated by DAPI –labeled nuclei) in the IPL and the number of Bhlhb5+ cells in the IPL and GCL per image (field of view is 291.2 μm of length). To determine the boundaries of the IPL and GCL, we used the DAPI images. For quantification of ectopic GFP+ or Abi1/2+ processes pointing to the INL, we counted the number of processes that emanate from an AC, as determined by its cell body position, and that point away from the IPL. To take into account the variability of the OMPL phenotype and be able to compare across genotypes, we calculated an "ectopic synapse score". For this, we assigned levels of OMPL formation: 0 (no OMPL), 1 (ectopic processes in INL), 2 (short stretches of OMPL) and 3 (longer than 100μm stretches of OMPL) per section of retina (Figures S4A–S4D). To incorporate all the phenotype intensities into one numerical value, we calculated an "ectopic synapses score" by averaging phenotype levels of each retinal section per animal and dividing by 3. Therefore, the phenotype ranged from score 0, where all sections in an animal would be normal, to score 1, where all sections would have a level 1 of phenotype. To quantify fluorescence intensity on immunohistochemistry samples we used Fiji (ImageJ) to measure the Mean Gray Value on areas of the IPL by tracing a rectangle that took up most of the IPL height. In addition, the Mean Gray Value was measured on a rectangle traced on the upper INL (where bipolar cell somas reside) and was used to normalize the value of the IPL. To quantify expression of transcripts by RNAscope, the images were thresholded until only puncta signal was observed. All images were treated the same way using Fiji (ImageJ). Then, the integrated density was measured to quantify total mRNA puncta in the same total area of each image (291.2 μm × 291.2 μm).

To determine significant differences between control and experimental groups, we used Prism6 software for statistical analysis. After applying a D'Agostino-Pearson omnibus normality test to determine Gaussian distribution of the samples, we either use two-tailed *t*

test (if the samples follow a Gaussian distribution) or Mann-Whitney test (if the samples did not follow a Gaussian distribution) to calculate the p values, except for Figure 6I where we used Fisher's exact test.

Supplementary Material

Refer to Web version on PubMed Central for supplementary material.

ACKNOWLEDGMENTS

REFERENCES

Avilés EC, and Goodrich LV (2017). Configuring a robust nervous system with Fat cadherins. Semin. Cell Dev. Biol 69, 91–101. [PubMed: 28603077]

Avilés EC, Krol A, Henle SJ, Burroughs-Garcia J, Deans MR, and Goodrich LV (2022a). Mass Spectrometry data for: Fat3 acts through independent cytoskeletal effectors to coordinate asymmetric cell behaviors during polarized circuit assembly. Harvard Dataverse, V1. 10.7910/DVN/TXMJYK.

Avilés EC, Krol A, Henle SJ, Burroughs-Garcia J, Deans MR, and Goodrich LV (2022b). "Source data for: Fat3 acts through independent cytoskeletal effectors to coordinate asymmetric cell behaviors during polarized circuit assembly". Harvard Dataverse, V1. 10.7910/DVN/AYEGN7.

Badouel C, Zander M, Liscio N, Bagherie-Lachidan M, Sopko R, Coyaud E, Raught B, Miller F, and McNeill H (2015). Fat1 interacts with Fat4 to regulate neural tube closure, neural progenitor proliferation and apical constriction during mouse brain development. Development 142, 2781–2791. [PubMed: 26209645]

Barlan K, Cetera M, and Horne-Badovinac S (2017). Fat2 and lar define a basally localized planar signaling system controlling collective cell migration. Dev. Cell 40, 467–477. [PubMed: 28292425]

Barnes AP, and Polleux F (2009). Establishment of axon-dendrite polarity in developing neurons. Annu. Rev. Neurosci 32, 347–381. [PubMed: 19400726]

Bear JE, and Gertler FB (2009). Ena/VASP: towards resolving a pointed controversy at the barbed end. J. Cell Sci 122, 1947–1953. [PubMed: 19494122]

Braun GS, Kretzler M, Heider T, Floege J, Holzman LB, Kriz W, and Moeller MJ (2007). Differentially spliced isoforms of FAT1 are asymmetrically distributed within migrating cells. J. Biol. Chem 282, 22823–22833. [PubMed: 17500054]

Brooun M, Klimovich A, Bashkurov M, Pearson BJ, Steele RE, and McNeill H (2020). Ancestral roles of atypical cadherins in planar cell polarity. Proc. Natl. Acad. Sci. U S A 117, 19310–19320. [PubMed: 32727892]

Cappello S, Gray MJ, Badouel C, Lange S, Einsiedler M, Srour M, Chitayat D, Hamdan FF, Jenkins ZA, Morgan T, et al. (2013). Mutations in genes encoding the cadherin receptor-ligand pair DCHS1 and FAT4 disrupt cerebral cortical development. Nat. Genet 45, 1300–1308. [PubMed: 24056717]

Caruso N, Herberth B, Bartoli M, Puppo F, Dumonceaux J, Zimmermann A, Denadai S, Lebossé M, Roche S, Geng L, et al. (2013). Deregulation of the protocadherin gene FAT1 alters muscle shapes: implications for the pathogenesis of facioscapulohumeral dystrophy. PLoS Genet. 9, e1003550. [PubMed: 23785297]

Chaya T, Ishikane H, Varner LR, Sugita Y, Maeda Y, Tsutsumi R, Mo-tooka D, Okuzaki D, and Furukawa T (2021). Deficiency of the neurodevelopmental disorder-associated gene Cyfip2 alters the retinal ganglion cell properties and visual acuity. Hum. Mol. Genet 10.1093/hmg/ddab268.

Chen B, Brinkmann K, Chen Z, Pak CW, Liao Y, Shi S, Henry L, Grishin NV, Bogdan S, and Rosen MK (2014a). The WAVE regulatory complex links diverse receptors to the actin cytoskeleton. Cell 156, 195–207. [PubMed: 24439376]

Chen XJ, Squarr AJ, Stephan R, Chen B, Higgins TE, Barry DJ, Martin MC, Rosen MK, Bogdan S, and Way M (2014b). Ena/VASP proteins cooperate with the WAVE complex to regulate the actin cytoskeleton. Dev. Cell 30, 569–584. [PubMed: 25203209]

Chen D-Y, Lipari KR, Dehghan Y, Streichan SJ, and Bilder D (2016). Symmetry breaking in an edgeless epithelium by fat2-regulated microtubule polarity. Cell Rep. 15, 1125–1133. [PubMed: 27134170]

Cheng H, Burroughs-Garcia J, Birkness JE, Trinidad JC, and Deans MR (2016). Disparate regulatory mechanisms control Fat3 and P75NTR protein transport through a conserved Kif5-interaction domain. PLoS One 11, e0165519. [PubMed: 27788242]

Chia PH, Chen B, Li P, Rosen MK, and Shen K (2014). Local F-actin network links synapse formation and axon branching. Cell 156, 208–220. [PubMed: 24439377]

Collin GB, Won J, Krebs MP, Hicks WJ, Charette JR, Naggert JK, and Nishina PM (2020). Disruption in murine Eml1 perturbs retinal lamination during early development. Sci. Rep 10, 5647. [PubMed: 32221352]

Deans MR, Krol A, Abraira VE, Copley CO, Tucker AF, and Goodrich LV (2011). Control of neuronal morphology by the atypical cadherin Fat3. Neuron 71, 820–832. [PubMed: 21903076]

Dosztanyi Z, Csizmok V, Tompa P, and Simon I (2005). IUPred: web server for the prediction of intrinsically unstructured regions of proteins based on estimated energy content. Bioinformatics 21, 3433–3434. [PubMed: 15955779]

Dubielecka PM, Ladwein KI, Xiong X, Migeotte I, Chorzalska A, Anderson KV, Sawicki JA, Rottner K, Stradal TE, and Kotula L (2011). Essential role for Abi1 in embryonic survival and WAVE2 complex integrity. Proc. Natl. Acad. Sci. U S A 108, 7022–7027. [PubMed: 21482783]

Fan L, Lu Y, Shen X, Shao H, Suo L, and Wu Q (2018). Alpha protocad-herins and Pyk2 kinase regulate cortical neuron migration and cytoskeletal dynamics via Rac1 GTPase and WAVE complex in mice. Elife 7, e35242. [PubMed: 29911975]

Fujitani Y, Fujitani S, Luo H, Qiu F, Burlison J, Long Q, Kawaguchi Y, Edlund H, MacDonald RJ, Furukawa T, et al. (2006). Ptf1a determines horizontal and amacrine cell fates during mouse retinal development. Development 133, 4439–4450. [PubMed: 17075007]

Fulford AD, and McNeill H (2020). Fat/Dachsous family cadherins in cell and tissue organisation. Curr. Opin. Cell Biol 62, 96–103. [PubMed: 31739265]

Furuta Y, Lagutin O, Hogan BLM, and Oliver GC (2000). Retina- and ventral forebrain-specific Cre recombinase activity in transgenic mice. Genesis 26, 130–132. [PubMed: 10686607]

Gee HY, Sadowski CE, Aggarwal PK, Porath JD, Yakulov TA, Schueler M, Lovric S, Ashraf S, Braun DA, Halbritter J, et al. (2016). FAT1 mutations cause a glomerulotubular nephropathy. Nat. Commun 7, 10822. [PubMed: 26905694]

Goodrich LV, and Strutt D (2011). Principles of planar polarity in animal development. Development 138, 1877–1892. [PubMed: 21521735]

Grove M, Demyanenko G, Echarri A, Zipfel PA, Quiroz ME, Rodriguiz RM, Playford M, Martensen SA, Robinson MR, Wetsel WC, et al. (2004). Abi2-Deficient mice exhibit defective cell migration, aberrant dendritic spine morphogenesis, and deficits in learning and memory. Mol. Cell. Biol 24, 10905–10922. [PubMed: 15572692]

Hirokawa N, Noda Y, Tanaka Y, and Niwa S (2009). Kinesin superfamily motor proteins and intracellular transport. Nat. Rev. Mol. Cell Biol 10, 682–696. [PubMed: 19773780]

Hou R, Liu L, Anees S, Hiroyasu S, and Sibinga NES (2006). The Fat1 cadherin integrates vascular smooth muscle cell growth and migration signals. J. Cell Biol 173, 417–429. [PubMed: 16682528]

Jossin Y (2020). Molecular mechanisms of cell polarity in a range of model systems and in migrating neurons. Mol. Cell. Neurosci 106, 103503. [PubMed: 32485296]

Krol A, Henle SJ, and Goodrich LV (2016). Fat3 and Ena/VASP proteins influence the emergence of asymmetric cell morphology in the developing retina. Development 143, 2172–2182. [PubMed: 27122175]

Lee H, Engel U, Rusch J, Scherrer S, Sheard K, and Van Vactor D (2004). The microtubule plus end tracking protein orbit/MAST/CLASP acts downstream of the tyrosine kinase Abl in mediating axon guidance. Neuron 42, 913–926. [PubMed: 15207236]

Linding R (2003). GlobPlot: exploring protein sequences for globularity and disorder. Nucleic Acids Res. 31, 3701–3708. [PubMed: 12824398]

Macosko EZ, Basu A, Satija R, Nemesh J, Shekhar K, Goldman M, Tirosh I, Bialas AR, Kamitaki N, Martersteck EM, et al. (2015). Highly parallel genome-wide expression profiling of individual cells using nanoliter droplets. Cell 161, 1202–1214. [PubMed: 26000488]

Mao Y, Mulvaney J, Zakaria S, Yu T, Morgan KM, Allen S, Basson MA, Francis-West P, and Irvine KD (2011). Characterization of a Dchs1 mutant mouse reveals requirements for Dchs1-Fat4 signaling during mammalian development. Development 138, 947–957. [PubMed: 21303848]

Matsuoka RL, Nguyen-Ba-Charvet KT, Parray A, Badea TC, Chédotal A, and Kolodkin AL (2011a). Transmembrane semaphorin signalling controls laminar stratification in the mammalian retina. Nature 470, 259–263. [PubMed: 21270798]

Matsuoka RL, Chivatakarn O, Badea TC, Samuels IS, Cahill H, Katayama K, Kumar SR, Suto F, Chédotal A, Peachey NS, et al. (2011b). Class 5 transmembrane semaphorins control selective mammalian retinal lamination and function. Neuron 71, 460–473. [PubMed: 21835343]

Miyazaki T (2011). Human FAT1 cadherin controls cell migration and invasion of oral squamous cell carcinoma through the localization of β-catenin. Oncol. Rep 26, 587–592. [PubMed: 21617878]

Moeller MJ, Soofi A, Braun GS, Li X, Watzl C, Kriz W, and Holzman LB (2004). Protocadherin FAT1 binds Ena/VASP proteins and is necessary for actin dynamics and cell polarization. EMBO J. 23, 3769–3779. [PubMed: 15343270]

Nagae S, Tanoue T, and Takeichi M (2007). Temporal and spatial expression profiles of the Fat3 protein, a giant cadherin molecule, during mouse development. Dev. Dyn 236, 534–543. [PubMed: 17131403]

Ray TA, Roy S, Kozlowski C, Wang J, Cafaro J, Hulbert SW, Wright CV, Field GD, and Kay JN (2018). Formation of retinal direction-selective circuitry initiated by starburst amacrine cell homotypic contact. Elife 7, e34241. [PubMed: 29611808]

Rocha-Martins M, Kretzschmar J, Nerli E, Weigert M, Icha J, Myers EW, and Norden C (2021). Bidirectional neuronal migration coordinates retinal morphogenesis by preventing spatial competition. BioRxiv. 10.1101/2021.02.08.430189.

Rottner K, Stradal TEB, and Chen B (2021). WAVE regulatory complex. Curr. Biol 31, R512–R517. [PubMed: 34033782]

Sadeqzadeh E, de Bock CE, and Thorne RF (2014). Sleeping giants: emerging roles for the fat cadherins in health and disease. Med. Res. Rev 34, 190–221. [PubMed: 23720094]

Squarr AJ, Brinkmann K, Chen B, Steinbacher T, Ebnet K, Rosen MK, and Bogdan S (2016). Fat2 acts through the WAVE regulatory complex to drive collective cell migration during tissue rotation. J. Cell Biol 212, 591–603. [PubMed: 26903538]

Sundararajan L, Norris ML, Schöneich S, Ackley BD, and Lundquist EA (2014). The fat-like cadherin CDH-4 acts cell-non-autonomously in anterior–posterior neuroblast migration. Dev. Biol 392, 141–152. [PubMed: 24954154]

Sundararajan L, Stern J, and Miller DM (2019). Mechanisms that regulate morphogenesis of a highly branched neuron in *C. elegans*. Dev. Biol 451, 53–67. [PubMed: 31004567]

Tanoue T, and Takeichi M (2004). Mammalian Fat1 cadherin regulates actin dynamics and cell–cell contact. J. Cell Biol 165, 517–528. [PubMed: 15148305]

Tsai RYL, and Reed RR (1997). Using a eukaryotic GST fusion vector for proteins difficult to express in *E. coli*. Biotechniques 23, 794–800. [PubMed: 9383538]

Urwyler O, Izadifar A, Vandenbogaerde S, Sachse S, Misbaer A, and Schmucker D (2019). Branch-restricted localization of phosphatase Prl-1 specifies axonal synaptogenesis domains. Science 364, eaau9952. [PubMed: 31048465]

Viktorinová I, and Dahmann C (2013). Microtubule polarity predicts direction of egg chamber rotation in Drosophila. Curr. Biol 23, 1472–1477. [PubMed: 23831293]

Viktorinová I, König T, Schlichting K, and Dahmann C (2009). The cadherin Fat2 is required for planar cell polarity in the Drosophila ovary. Development 136, 4123–4132. [PubMed: 19906848]

Xu C, Theisen E, Maloney R, Peng J, Santiago I, Yapp C, Werkhoven Z, Rumbaut E, Shum B, Tarnogorska D, et al. (2019). Control of synaptic specificity by establishing a relative preference for synaptic partners. Neuron 103, 865–877.e7. [PubMed: 31300277]

Yan W, Laboulaye MA, Tran NM, Whitney IE, Benhar I, and Sanes JR (2020). Mouse retinal cell atlas: molecular identification of over sixty amacrine cell types. J. Neurosci 40, 5177–5195. [PubMed: 32457074]

Zakaria S, Mao Y, Kuta A, Ferreira de Sousa C, Gaufo GO, McNeill H, Hindges R, Guthrie S, Irvine KD, and Francis-West PH (2014). Regulation of neuronal migration by Dchs1-Fat4 planar cell polarity. Curr. Biol 24, 1620–1627. [PubMed: 24998526]

Zou Y (2020). Breaking symmetry – cell polarity signaling pathways in growth cone guidance and synapse formation. Curr. Opin. Neurobiol 63, 77–86. [PubMed: 32361599]

Highlights

- The Fat3 intracellular domain binds cytoskeletal regulators and synaptic proteins

- Expression of Fat3 isoforms switches over the course of retinal development

- Fat3 controls cell migration and neurite retraction via discrete intracellular motifs

- Fat3 can influence synapse development independently of effects on neurite retraction
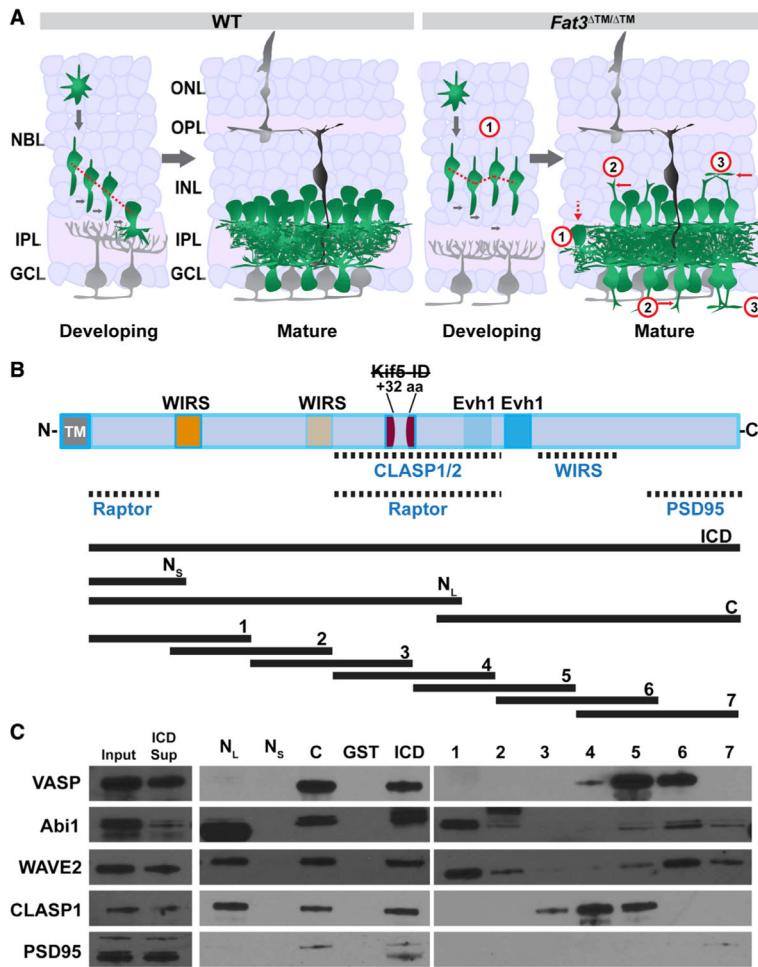
Figure 1. The Fat3-ICD interacts with multiple cytoskeletal effectors

(A) Summary of Fat3's effects on mouse retinal development. Wild-type (WT) ACs (green) migrate smoothly through the neuroblast layer (NBL) toward the inner nuclear layer (INL). In *Fat3* $^{\Delta TM/\Delta TM}$ mutants, (1) neuronal migration is affected with more ACs that halt in the inner plexiform layer (IPL) or that migrate into the ganglion cell layer (GCL), (2) neurite retraction is unreliable, and (3) ectopic synapses form in the INL and below the GCL. ONL, outer nuclear layer; OPL, outer plexiform layer.

(B) Known and predicted binding sites in the Fat3-ICD, with newly defined sites marked with dotted lines. Solid lines represent fragments tiling the ICD that were used for GST pull-downs.

(C) Western blots after GST pull-down from brain lysate using GST fusions to the fragments in (B) (N_S, N_L, C, ICD, 1–7) or GST-only controls. All binding partners were present in brain lysate before pull down (input), with reduced levels detected in the ICD supernatant (ICD Sup) after pull down, consistent with efficient depletion.

See also Figure S1 and Tables S1 and S2.
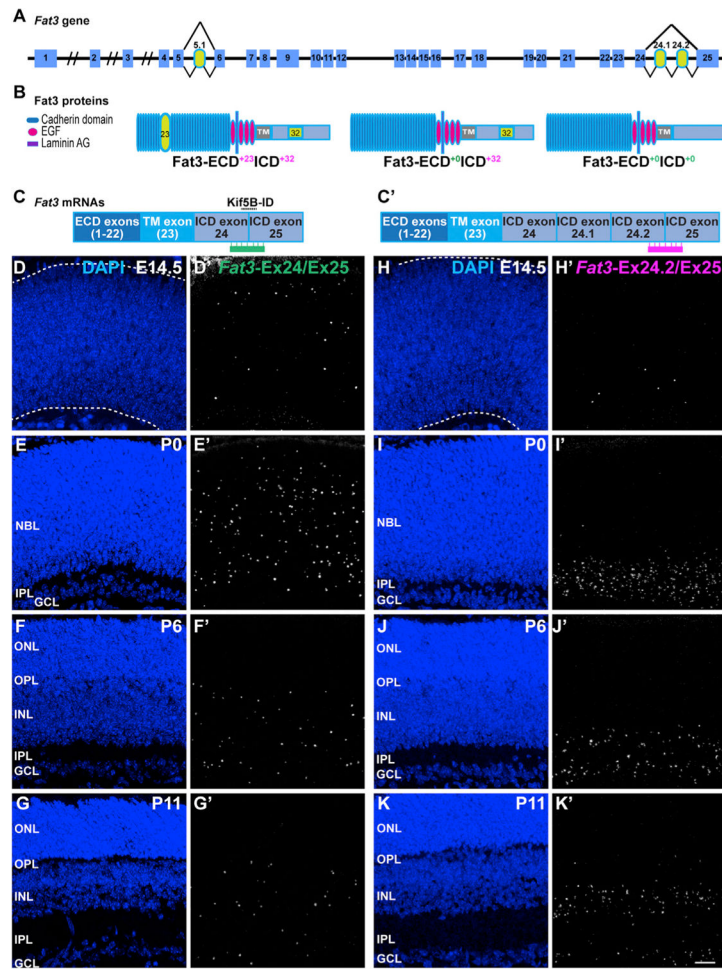
Figure 2. Differential expression of two Fat3-ICD isoforms in the developing retina

(A) Diagram of the *Fat3* gene structure illustrating alternative splicing events.

(B) Three different isoforms of Fat3 can be produced in the P0 retina.

(C) Diagram of *Fat3* mRNA illustrating where Basescope *in situ* probes bind splice junctions to distinguish alternative splice isoforms.

(D–K′) Basescope *in situ* hybridization on retinal sections at E14.5, P0, P6, and P11 using isoformspecific probes to track Fat3-ICD isoform expression during retinal development. Scale bar: 20 µm.

See also Figure S2 and Tables S3 and S4.
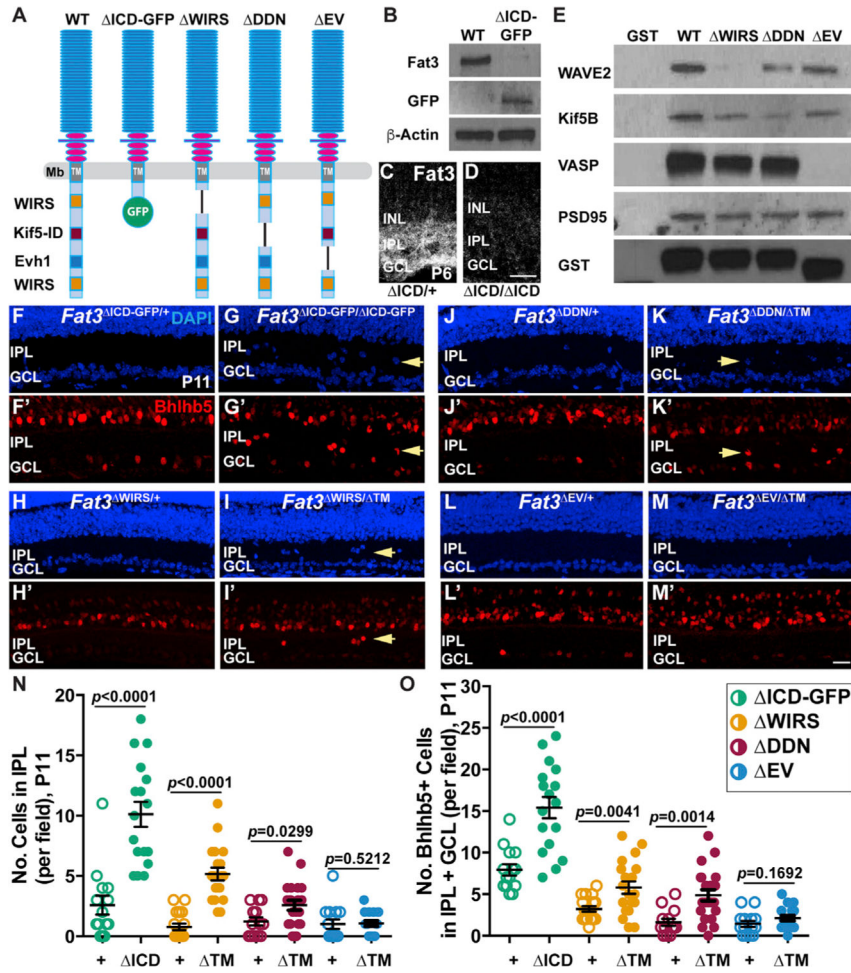
Figure 3. A subset of motifs in the Fat3-ICD are required for AC migration

(A) Schematic representations of Fat3-ICD mutants used in this study (not to scale).

(B) Western blot using antibodies to the Fat3-ICD and GFP confirms that $Fat3^{ICD-GFP}$ mice produce a Fat3-GFP fusion protein that lacks the ICD. β-actin was used as a loading control.

(C and D) Anti-Fat3 staining of $Fat3^{ICD-GFP/+}$ (C) and $Fat3^{ICD-GFP/ICD-GFP}$ (D) retinas. The antibody recognizes the Fat3-ICD.

(E) GST pull-down from brain lysates shows selective loss of predicted binding partners for each mutant protein, with retention of PSD95 binding in all cases.

(F–K′) DAPI and anti-Bhlhb5 staining of P11 retinal sections reveal AC migration defects in $Fat3^{ICD-GFP/ICD-GFP}$ (N = 3, n = 17), $Fat3^{WIRS/TM}$ (N = 4, n = 19), and $Fat3^{DDN/TM}$ mutants (N = 4, n = 21) compared with in $Fat3^{ICD-GFP/+}$ (N = 3, n = 14), $Fat3^{WIRS/+}$ (N = 4, n = 18), and $Fat3^{DDN/+}$ (N = 4, n = 13) controls, respectively. Arrows point to mislocalized AC somas in the IPL.

(L–M′) By contrast, migration is unaffected in $Fat3^{EV/TM}$ mice (N = 3, n = 17) compared with in $Fat3^{EV/+}$ controls (N = 3, n = 14).

(N and O) Quantification of DAPI-stained nuclei in the IPL (N) and Bhlhb5+ nuclei in the IPL and GCL (O). t test was used for all comparisons except $Fat3^{ICD-GFP/+}$ versus $Fat3^{ICD-GFP/ICD-GFP}$ in (N) and (O) and $Fat3^{EV/+}$ vs $Fat3^{EV/TM}$ in (N), which were by

Mann–Whitney test. Scale bars: 20 μm. Each field is 291.2 μm long. Data are represented as mean ± SEM.

See also Figure S3.
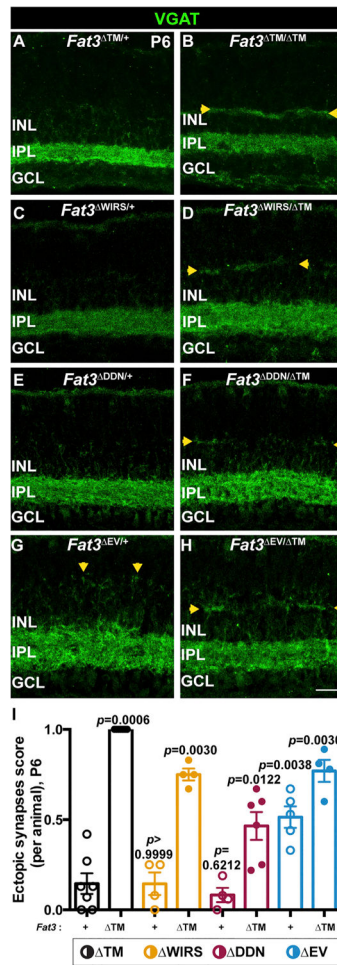
Figure 4. The WIRS, Kif5-ID, and Evh1 motifs are required for proper synapse localization

(A–H) Anti-VGAT staining of *Fat3* $^{\Delta TM/+}$ (A), *Fat3* $^{\Delta TM/\Delta TM}$ (B), *Fat3* $^{\Delta WIRS/+}$ (C), *Fat3* $^{\Delta WIRS/\Delta TM}$ (D), *Fat3* $^{\Delta DDN/+}$ (E), *Fat3* $^{\Delta DDN/\Delta TM}$ (F), *Fat3* $^{\Delta EV/+}$ (G), and *Fat3* $^{\Delta EV/\Delta TM}$ (H) mutant retinal sections at P6. Arrows point to the OMPL.

(I) Quantification of ectopic synapse scores in *Fat3* $^{\Delta TM/+}$ (N = 7, n = 34) versus *Fat3* $^{\Delta TM/\Delta TM}$ (N = 7, n = 28), *Fat3* $^{\Delta WIRS/+}$ (N = 4, n = 16), *Fat3* $^{\Delta WIRS/\Delta TM}$ (N = 4, n = 16), *Fat3* $^{\Delta DDN/+}$ (N = 4, n = 23), *Fat3* $^{\Delta DDN/\Delta TM}$ (N = 6, n = 30), *Fat3* $^{\Delta EV/+}$ (N = 5, n = 18), and *Fat3* $^{\Delta EV/\Delta TM}$ (N = 4, n = 21) mutants. Mann–Whitney test was used. Scale bar: 20 μm. Data are represented as mean ± SEM.

See also Figures S4 and S5.
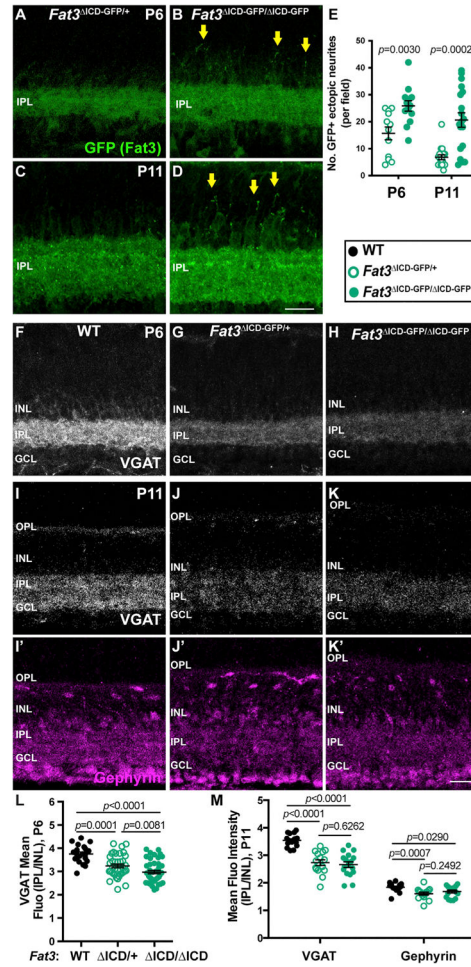
Figure 5. Independent effects of Fat3 on neurite retraction and synapse formation

(A–E) Anti-GFP staining of retinal sections at P6 (A and B) and P11 (C and D) reveals Fat3-GFP in the IPL of *Fat3* [ICD–GFP] heterozygotes (A and C) and homozygotes (B and D), where Fat3 is known to localize (Deans et al., 2011). In addition, Fat3 [ICD–GFP] localizes to the tips of unretracted AC neurites in the INL (arrows, B and D) of *Fat3* [ICD–GFP/ ICD–GFP] mutants, quantified in (E). *Fat3* [ICD–GFP/+] (P6: N = 4, n = 12; P11: N = 3, n = 18) and *Fat3* [ICD–GFP/ ICD–GFP] (P6: N = 4, n = 13; P11: N = 3, n = 19) retinas. t test was applied to P6 data, and Mann-Whitney test was applied to P11 data.

(F–K) Anti-VGAT (F–K) and anti-Gephyrin (I′–K′) staining of WT (F and I), *Fat3* [ICD–GFP/+] (G and J), and *Fat3* [ICD–GFP/ ICD–GFP] (H and K) retinas at P6 (F–H) and P11 (I–K) shows that no ectopic synapses form in *Fat3* [ICD–GFP/ ICD–GFP] mutants despite the presence of many GFP+ ectopic neurites (E). However, VGAT intensity in the IPL is significantly reduced in P6 and P11 heterozygotes (G and J) and homozygotes (H and K). At P11, Gephyrin intensity (I′, J′, and K′) is also decreased.

(L) Quantification of mean VGAT fluorescence intensity in IPL normalized to upper INL at P6 for WT (N = 4, n = 21), *Fat3* [ICD–GFP/+] (N = 8, n = 38), and *Fat3* [ICD–GFP/ ICD–GFP] (N = 9, n = 44) retinas. Mann–Whitney test was used.

(M) Quantification of VGAT and Gephyrin intensity in the IPL of WT (N = 3, n = 15), *Fat3* [ICD–GFP/+] (N = 3, n = 15), and *Fat3* [ICD–GFP/ ICD–GFP] (N = 3, n = 17) at P11. t test

was used for VGAT intensity, and Mann Whitney test was used for Gephyrin intensity. Scale bars: 20 μm. Each field is 291.2 μm long. Data are represented as mean ± SEM.

See also Figure S6.
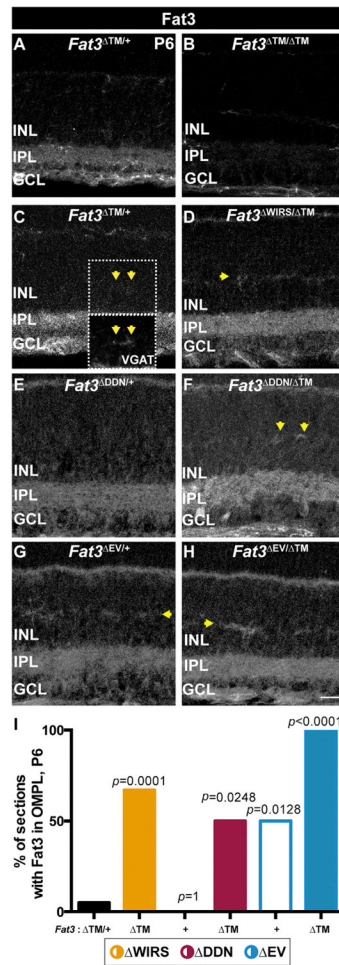
Figure 6. Mutant Fat3 proteins mislocalize to the INL

(A–C) Anti-Fat3 staining of P6 *Fat3* ^{ΔTM/+} (A and C) retinal sections shows that WT Fat3 is localized to the IPL, even in regions where ectopic VGAT+ neurites form a patch of OMPL (arrows, bottom inset, C). No signal is detected in *Fat3* ^{ΔTM/ΔTM} homozygotes (B), confirming that the signal corresponds to Fat3.

(D–H) Anti-Fat3 staining of P6 *Fat3* ^{ΔWIRS/ΔTM} (D), *Fat3* ^{ΔDDN/+} (E), *Fat3* ^{ΔDDN/ΔTM} (F), *Fat3* ^{ΔEV/+} (G), and *Fat3* ^{ΔEV/ΔTM} (H) retinal sections, with arrows indicating mislocalization to the OMPL (D and F–H).

(I) Quantification of Fat3 mislocalization. The bars represent the percentage of retinal sections with evidence of Fat3 in the OMPL. Fisher's exact test was used. Scale bar: 20 μm.
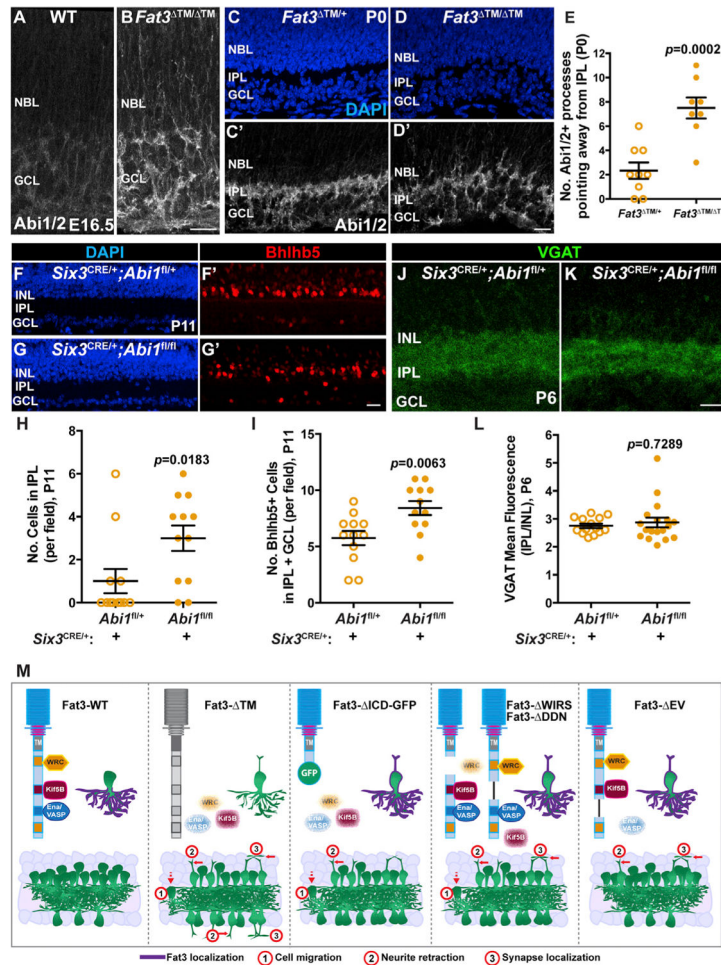
Figure 7. Fat3 localizes WRC components that are essential for AC migration

(A and B) Anti-Abi1/2 immunostaining of E16.5 WT

(A) and *Fat3* $^{\Delta TM/\Delta TM}$ (B) retinas shows a change in Abi1/2 localization in the absence of Fat3.

(C–E) In P0 *Fat3* $^{\Delta TM/+}$ retinas (C′), Abi1/2 is enriched in the nascent IPL. By contrast, significantly more Abi1/2+ processes point away from the IPL in *Fat3* $^{\Delta TM/\Delta TM}$ retinas (D′) (7.50 ± 0.86 processes per field, N = 3, n = 8) than in *Fat3* $^{\Delta TM/+}$ controls (2.33 ± 0.66 processes per field, N = 3, n = 9, p = 0.0002, t test), quantified in (E).

(F–G′) Anti-Bhlhb5 and DAPI staining of retinal sections from P11 control (F) and *Abi1* cKO homozygotes (G) reveals AC migration defects.

(H) Quantification of nuclei in the IPL for *Six3* $^{CRE/+}$; *Abi1* $^{fl/+}$ (N = 3, n = 12) and *Six3* $^{CRE/+}$;*Abi1* $^{fl/fl}$ (N= 3, n = 12). Mann–Whitney test was used.

(I) Quantification of Bhlhb5+ cells in the IPL and GCL. t test was used.

(J and K) Deletion of *Abi1* from the retina does not induce ectopic synapses, as seen by anti-VGAT staining of P6 control (*Six3* $^{CRE/+}$;*Abi1* $^{fl/+}$) and mutant (*Six3* $^{CRE/+}$;*Abi1* $^{fl/fl}$) retinal sections.

(L) Quantification of mean VGAT fluorescence intensity in IPL normalized to upper INL for *Six3* $^{CRE/+}$; *Abi1* $^{fl/+}$ (N = 3, n = 14) and *Six3* $^{CRE/+}$;*Abi1* $^{fl/fl}$ (N= 4, n = 18) retinas. Mann–Whitney test was used. Scale bars: 20 μm. Each field is 291.2 μm long.

(M) Diagrams summarizing the key findings of this study. Data are represented as mean ± SEM.

See also Figure S7.

KEY RESOURCES TABLE

REAGENT or RESOURCE	SOURCE	IDENTIFIER
Antibodies		
Mouse anti Abi1	MBL	Cat#D147–3, clone 1B9; RRID:AB_592744
Rabbit anti Abi1/2	Thermo Fisher Scientific	Cat#PA5–78705, RRID:AB_2745821
Rabbit anti beta-actin	Raybiotech	Cat#168–10656; RRID:AB_2885189
Goat anti Bhlhb5	Santa Cruz	Cat#sc-6045; RRID:AB_2065343
Rat anti CLASP1	Absea	Cat#050801A06; RRID:AB_2885190
Rat anti CLASP2	Absea	Cat#032012H02; RRID:AB_2885191
Mouse anti Fat3	This study	RRID: AB_2904260
Rabbit anti Fat3	Deans et al. (2011)	RRID: AB_2904259
Mouse anti Gephyrin	Synaptic Systems	Cat#147 011; RRID:AB_887716
Chicken anti GFP	Aves	Cat#GFP-1020; RRID:AB_10000240
Goat anti GFP-FITC	Abcam	Cat#ab6662; RRID:AB_305635
Rabbit anti GST	Cell signaling	Cat#2625S; RRID:AB_490796
Goat anti Kif5B	Imgenex	Cat#IMG-3049; RRID:AB_317079
Rabbit anti Pax6	Biolegend	Cat#901301; RRID:AB_2565003
Rabbit anti PDS95	Abcam	Cat#ab18258; RRID:AB_444362
Rabbit anti Raptor	Cell signaling	Cat#2280; RRID:AB_561245
Rabbit anti VASP	Gertler lab, MIT	N/A
Rabbit anti VGAT	Synaptic systems	Cat#131002; RRID:AB_887871
Rabbit anti WAVE2	Cell signaling	Cat# 3659; RRID:AB_2216981
Donkey anti chicken, Alexa Fluor® 488	Jackson ImmunoResearch	Cat#703-545-155; RRID:AB_2340375
Goat anti chicken, Alexa Fluor® 488	Thermo Fisher Scientific	Cat# A-11039; RRID:AB_142924
Donkey anti goat, Alexa Fluor® 568	Thermo Fisher Scientific	Cat#A11057; RRID:AB_142581
Donkey anti mouse, Alexa Fluor® 488	Abcam	Cat#ab150105; RRID:AB_2732856
Donkey anti mouse, Alexa Fluor® 568	Thermo Fisher Scientific	Cat#A10037; RRID:AB_2534013
Goat anti mouse, Alexa Fluor® 647	Thermo Fisher Scientific	Cat#A-21235; RRID:AB_2535804
Donkey anti rabbit, Alexa Fluor® 488	Thermo Fisher Scientific	Cat#A21206; RRID:AB_2535792
Donkey anti rabbit, Alexa Fluor® 568	Thermo Fisher Scientific	Cat#A10042; RRID:AB_2534017
Donkey anti rabbit, Alexa Fluor® 647	Thermo Fisher Scientific	Cat#A31573; RRID:AB_2536183
Goat anti rat, HRP	Thermo Fisher Scientific	Cat#31470; RRID:AB_228356
Goat anti mouse, HRP	Bio-Rad	Cat#170–6516; RRID:AB_11125547
Rabbit anti goat, HRP	Bio-Rad	Cat#172-1034; RRID:AB_11125144
Goat anti rabbit, HRP	Bio-Rad	Cat#170–6515; RRID:AB_11125142
Bacterial and virus strains		
Rosetta™ (DE3) Competent Cells	Sigma Millipore	Cat#70954
One Shot™ TOP10 Chemically Competent *E. coli*	Thermo Fisher Scientific	Cat#C404010

REAGENT or RESOURCE	SOURCE	IDENTIFIER
Critical commercial assays		
RNAscope® Multiplex Fluorescent Reagent Kit v2	ACD	Cat#323100
BaseScope™ Reagent Kit v2- RED	ACD	Cat#323910
Deposited data		
Mass spectrometry dataHarvardData	Harvard Dataverse (Avilés et al., 2022a)	DOI: https://doi.org/10.7910/DVN/TXMJYK
Source dataHarvardData	Harvard Dataverse (Avilés et al., 2022b)	DOI: https://doi.org/10.7910/DVN/AYEGN7
Experimental models: cell lines		
HEK293 cells	ATCC	Cat#CRL-1573
Experimental models: organisms/strains		
Mouse: $Six3^{Cre}$	Jackson lab (Furuta et al., 2000)	Cat#019755
Mouse: $Ptf1a^{Cre}$	Fujitani et al. (2006)	N/A
Mouse: Fat1^floxed	Caruso et al. (2013)	N/A
Mouse: $Abi1^{floxed}$	Dubielecka et al. (2011)	N/A
Mouse: $Fat3D^{TM}$	Deans et al. (2011)	N/A
Mouse: $Fat3^{ICD-GFP}$	This paper	N/A
Mouse: $Fat3^{WIRS}$	This paper	N/A
Mouse: $Fat3^{DDN}$	This paper	N/A
Mouse: $Fat3^{EV}$	This paper	N/A
Oligonucleotides		
EA41 (F): TGACGATCAAGGCTGTGGACA	This paper	N/A
EA67 (R): GCTTCGTGGTCCAGTCTCTC	This paper	N/A
EA68 (R): CGGTTGTAATTCTGTCCTTGGT	This paper	N/A
EA69 (R): CTGGTCAGGGAAGTCCTCAG	This paper	N/A
EA70 (F): AGACAGCTTGTGGGCAGAAC	This paper	N/A
EA71 (F): GACATCGTCGGGGGGGAAT	This paper	N/A
EA99 (F): CTCAGACTGCGACTCCATCC	This paper	N/A
EA100 (R): GGCTCTCATAGTTGGGCATT	This paper	N/A
Recombinant DNA		
pGEX6P-1-GST	Sigma Millipore	Cat#GE28-9546-48
pGEX6P-1-GST-Fat3-ICD	This paper	N/A
pGEX6P-1-GST-Fat3-ICD-N_L	This paper	N/A
pGEX6P-1-GST-Fat3-ICD-N_S	This paper	N/A
pGEX6P-1-GST-Fat3-ICD-C	This paper	N/A
pGEX6P-1-GST-Fat3-ICD-1	This paper	N/A
pGEX6P-1-GST-Fat3-ICD-2	This paper	N/A
pGEX6P-1-GST-Fat3-ICD-3	This paper	N/A
pGEX6P-1-GST-Fat3-ICD-4	This paper	N/A
pGEX6P-1-GST-Fat3-ICD-5	This paper	N/A
pGEX6P-1-GST-Fat3-ICD-6	This paper	N/A

REAGENT or RESOURCE	SOURCE	IDENTIFIER
pGEX6P-1-GST-Fat3-ICD-7	This paper	N/A
pCMV-GST	Tsai and Reed (1997)	N/A
pCMV-GST-Fat3-ICD	This paper	N/A
pCMV-GST-Fat3-ICD- WIRS	This paper	N/A
pCMV-GST-Fat3-ICD- DDN	This paper	N/A
pCMV-GST-Fat3-ICD- EV	This paper	N/A
Other		
In situ hybridization probe: RNAscope® Probe- Mm-Fat3-O1	ACD	Cat# 509051
In situ hybridization probe: RNAscope® Probe- Mm-Fat1-O1-C2	ACD	Cat# 509041-C2
In situ hybridization probe: RNAscope® Probe - Mm-Abi1-O1-C2	ACD	Cat# 567481-C2
In situ hybridization probe: BA-Mm-Fat3-x1-E6E7	ACD	Cat# 705311
In situ hybridization probe: BA-Mm-Fat3-E5E6	ACD	Cat# 709961
In situ hybridization probe: BA-Mm-Fat3-x1 -E25E26	ACD	Cat# 708501
In situ hybridization probe: BA-Mm-Fat3-E24E25	ACD	Cat# 709971